AGU PUBLICATIONS

JGR

Journal of Geophysical Research: Atmospheres

RESEARCH ARTICLE
10.1002/2016JD026357

Information content of visible and midinfrared radiances for retrieving tropical ice cloud properties

Kai-Wei Chang[1], **Tristan S. L'Ecuyer**[1], **Brian H. Kahn**[2], **and Vijay Natraj**[2]

[1]Department of Atmospheric and Oceanic Sciences, University of Wisconsin-Madison, Madison, Wisconsin, USA, [2]Jet Propulsion Laboratory, California Institute of Technology, Pasadena, California, USA

Key Points:
- An optimal combination of AIRS and MODIS observations for ice cloud retrievals are identified using information content and clustering analysis
- Shortwave infrared (near 4 μm) channels are most favored for both instruments, due to their sensitivity to optical depth and particle size
- Cloud boundary a priori assumptions were found to significantly influence the channel selection

Correspondence to:
K.-W. Chang,
kchang37@wisc.edu

Citation:
Chang, K.-W., T. S. L'Ecuyer, B. H. Kahn, and V. Natraj (2017), Information content of visible and midinfrared radiances for retrieving tropical ice cloud properties, *J. Geophys. Res. Atmos.*, *122*, doi:10.1002/2016JD026357.

Received 18 JAN 2017
Accepted 19 APR 2017
Accepted article online 25 APR 2017

Abstract Hyperspectral instruments such as Atmospheric Infrared Sounder (AIRS) have spectrally dense observations effective for ice cloud retrievals. However, due to the large number of channels, only a small subset is typically used. It is crucial that this subset of channels be chosen to contain the maximum possible information about the retrieved variables. This study describes an information content analysis designed to select optimal channels for ice cloud retrievals. To account for variations in ice cloud properties, we perform channel selection over an ensemble of cloud regimes, extracted with a clustering algorithm, from a multiyear database at a tropical Atmospheric Radiation Measurement site. Multiple satellite viewing angles over land and ocean surfaces are considered to simulate the variations in observation scenarios. The results suggest that AIRS channels near wavelengths of 14, 10.4, 4.2, and 3.8 μm contain the most information. With an eye toward developing a joint AIRS-MODIS (Moderate Resolution Imaging Spectroradiometer) retrieval, the analysis is also applied to combined measurements from both instruments. While application of this method to MODIS yields results consistent with previous channel sensitivity studies, the analysis shows that this combination may yield substantial improvement in cloud retrievals. MODIS provides most information on optical thickness and particle size, aided by a better constraint on cloud vertical placement from AIRS. An alternate scenario where cloud top boundaries are supplied by the active sensors in the A-train is also explored. The more robust cloud placement afforded by active sensors shifts the optimal channels toward the window region and shortwave infrared, further constraining optical thickness and particle size.

1. Introduction

Clouds regulate the Earth's climate or energy balance through interactions with solar and terrestrial radiation [*Liou*, 1986]. Cirrus on average cover 16.7% of the globe, and about 35% of cirrus clouds are found in the tropics within 15° of the equator [*Sassen et al.*, 2008, 2009]. In addition to radiatively influencing the climate, tropical cirrus is also linked to the amount of water vapor entering the stratosphere [*Brewer*, 1949; *Jensen et al.*, 1996]. Accurate representations of ice clouds are, therefore, necessary to accurately constrain climate processes in models. Furthermore, the manner in which clouds interact with the radiation field depends on their macrophysical and microphysical properties, including water path, particle size, geometric thickness, and height. These properties, in turn, define the cloud's shortwave albedo, longwave emissivity, and optical thickness which are fundamental to its radiative impacts. For this reason, much effort has been devoted to retrieving these parameters from a variety of satellite remote sensors, as well as surface-based observations and aircraft in situ sampling.

Passive sensors such as the Atmospheric InfraRed Sounder (AIRS) [*Aumann et al.*, 2003] and the Moderate Resolution Imaging Spectroradiometer (MODIS) [*Barnes et al.*, 1998] have accumulated over a decade-long record of observations that is particularly valuable for evaluating clouds in the context of climate processes and interannual variations. Several retrieval techniques have been developed to make use of these observations for estimating cloud properties. For example, the split-window technique [*Inoue*, 1985] retrieves cloud optical thickness and effective particle size by a lookup-table approach using brightness temperatures in the window region. For optically thicker clouds, the Nakajima-King approach [*Nakajima and King*, 1990] also retrieves optical thickness and effective particle size using a nonabsorbing channel in the visible band and an absorbing channel in the near-infrared (NIR) region. For retrieving cloud top temperature, the CO_2 slicing method [*Smith and Platt*, 1978] utilizes channels within 13–15 μm to vertically position the cloud and

is effective particularly for optically thin clouds. More recently, a number of approaches have also been developed for retrieving cloud macrophysical and microphysical properties simultaneously. One technique that is often adopted for this purpose is optimal estimation (OE) [*Rodgers*, 1976], which obtains an estimate that maximizes the a posteriori probability of the joint probability distribution between a priori estimates and the observations. OE has been effectively applied to global cloud retrievals using independent observations from MODIS [*Cooper et al.*, 2007; *Wang et al.*, 2016a] and AIRS [*Kahn et al.*, 2014].

Maximizing the value of combining MODIS and AIRS observations requires careful consideration of the synergies between these instruments to improve and refine the state of passive retrieval techniques. In principle, OE provides a framework for optimally combining information from multiple instruments since it allows for any number of observations, or bands/channels, given that one can appropriately model the observations, their Jacobians, and the associated uncertainties. However, in practice, modeling the satellite-observed radiances and their Jacobians can be computationally expensive. As such, it is desirable to restrict the retrieval to use only the channels most sensitive to the desired atmospheric state. Such channel selection is particularly important for hyperspectral sensors like AIRS, due to the large number of channels (2378), additional computational expense to calculating radiances at finer resolution ($\sim$1 cm^{-1}), and the varying influence of other parameters such as atmospheric temperature and humidity on each channel. There is, therefore, a need for objectively selecting optimal channel sets for cloud retrievals that maximize information while minimizing computation time. An objective way of determining the most crucial channels is through quantifying changes in information content (IC).

IC can be understood by recognizing that the problem of retrieving cloud properties is an inverse problem in which the range of possible states is characterized by a probability distribution. Upon obtaining a measurement, the range of probable states is generally reduced. The IC represents the magnitude of such reduction. More specifically, given a set of Jacobians that represent the sensitivity of the observations (radiances) to the retrieval variable, and the observation errors (noise, bias, etc.), IC represents the capability of an observation to reduce the width of the a priori probability density function (PDF) of possible states. Applied to spectral channels of spectrometers, this quantity naturally represents the impact of each channel on the retrieval. For this reason, IC plays a central role in channel selection methodologies [*Rodgers*, 1996]. *Sofieva* [2003] demonstrated an IC channel selection approach on measurements from the Global Ozone Monitoring by Occultation of Stars stellar occultation instrument for finding optimal channel combinations to retrieve atmospheric optical thickness. The selections of optimal MODIS channels for the retrieval of liquid or ice cloud properties respectively, were reported in *L'Ecuyer et al.* [2006] and *Cooper et al.* [2006]. *Sourdeval et al.* [2015] utilized IC to analyze the feasibility of retrieving cloud properties in multilayer cloud configurations. An IC channel analysis was employed by *Wang et al.* [2016b] to diagnose MODIS channels in an optimal estimation retrieval.

Several sensitivity studies have examined the effectiveness of infrared radiances for retrieving ice cloud properties. *Chung et al.* [2000] analyzed the sensitivity of high-resolution midinfrared radiances to ice cloud particle size, ice water path, cloud top position, and thickness by varying these cloud properties in radiative transfer simulations, while *Huang et al.* [2004] adopted a similar approach to examine the sensitivity of IR radiances toward cloud optical thickness and particle size. *Kahn et al.* [2004] employed a statistical approach using empirical orthogonal function analysis to examine the variance of midinfrared radiances due to varying ice crystal shape, effective radius, ice water path, as well cloud height and thickness.

Similar to such approaches, IC analysis also considers the channel sensitivities through the Jacobian, but has the added advantage of including multiple error sources, especially those associated with forward modeling. In addition, IC analysis is especially compatible with optimal estimation, as it considers the error covariances of the a priori estimates.

In this study we apply an IC-based channel selection to identify the optimal set of AIRS channels for cloud property retrievals under three scenarios: a stand-alone AIRS algorithm, a combined AIRS-MODIS algorithm, and a combined active/passive retrieval that further utilizes cloud boundary information from CloudSat and CALIPSO. AIRS is a hyperspectral infrared spectrometer on board the Aqua satellite with 2378 channels over wavelengths of 3.74–4.61 μm, 6.20–8.22 μm, and 8.8–15.4 μm [*Aumann et al.*, 2003]. Its spatial resolution is 13.5 km by 13.5 km at nadir and 41 km by 21.4 km at the scan extremes. The AIRS version 6 ice cloud retrieval product is derived from an OE algorithm, providing estimates of the cloud thermodynamic phase, effective diameter (D_e), cloud optical thickness (COT), and cloud top temperature (T_c) at the AIRS footprint resolution

[*Kahn et al.*, 2014]. The OE algorithm is applied to the 27% of AIRS fields of view that are identified as containing an ice cloud thermodynamic phase [*Jin and Nasiri*, 2014; *Kahn et al.*, 2015]. This algorithm uses 59 channels located within 8–15 μm, selected to include three spectral regions: CO_2 slicing channels within 13.2–14.5 μm, and the window regions between 10–12 μm and 8.8–9.15 μm, manually picked by avoiding strong absorption lines and noisy channels. Although these spectral regions have been shown to have sensitivity to the aforementioned cloud properties [*Huang et al.*, 2004], the channels were not optimized through a rigorous objective channel selection methodology. Also, it is known that some channels are specifically useful for certain types of clouds. For instance, the 13–15 μm region is effective for obtaining cloud top temperature of optically thin clouds [*Smith and Platt*, 1978], whereas for optically thick clouds, such as anvil tops, the 11 μm brightness temperature is often used as a proxy for its physical temperature.

Here we apply a formal channel selection process to a variety of ice clouds objectively extracted using a clustering algorithm on a database of cloud retrievals from observations of ground radar/lidars deployed by the U. S. Department of Energy Atmospheric Radiation Measurement (ARM) program [*Ackerman and Stokes*, 2003]. This diverse collection of cloud states spans a wide range of optical and geometrical thicknesses, particle size distributions, and heights, allowing optimal channels to be selected for a range of scenes appropriate for retrievals over the tropics. Satellite viewing geometry is considered through simulations at seven different viewing angles. Ocean, vegetation, and bare soil surfaces are examined separately to quantify the difference in optimal channel configuration over distinct land and ocean surfaces. Through considerations of the above factors and appropriate representations of forward model uncertainties, it is anticipated that the resulting AIRS channel set will be optimal for ice cloud retrievals in most scenarios. In addition to AIRS, IC channel selection is also applied to MODIS, to gain insight into how the two instruments can be jointly used for ice cloud retrievals.

While the wide swaths of AIRS and MODIS provide important sampling, it has been demonstrated that passive cloud retrievals can benefit from the more precise delineation of cloud boundaries afforded by active sensors. *Cooper et al.* [2003], for example, showed that having accurate cloud boundary information (cloud top temperature or height) can reduce the error in retrieved particle size and COT. Conversely, the lack of accurate boundary information can cause large errors. Thus, in addition to exploring an optimized AIRS channel selection, this study also explores the scenario where passive retrievals may further leverage cloud boundary information from active radar/lidar measurements. Both AIRS and MODIS fly aboard the Aqua satellite in the A-Train constellation, which includes CloudSat and CALIPSO. These sensors have obtained multiple years of collocated observations valuable for extracting high-quality estimates of cloud properties. In this paper, we examine the impacts of having CloudSat cloud top boundary on the optimal passive channels for ice cloud retrievals.

Section 2 describes the cloud database and our method for extracting ice cloud types using an established clustering algorithm. Section 3 provides an overview of the radiative transfer model, its atmospheric inputs, and the IC selection methodology. Channel selection results for independent AIRS and MODIS retrievals, combined AIRS+MODIS retrievals, and combined active-passive retrievals are discussed in section 4. The concluding section 5 summarizes all results and supplies a recommended channel set and their possible applications.

2. Ice Cloud Database Construction

To account for the dynamic range of ice cloud properties found in the tropics, the IC of all AIRS and MODIS channels must be evaluated over a wide range of ice cloud types. The ARM program [*Ackerman and Stokes*, 2003] has deployed active ground-based sensors at multiple stationary sites in the Tropical Western Pacific (TWP), Lamont, Oklahoma, and in Barrow, Alaska. For the three TWP sites, the "Cloud Properties and Radiative Heating Rates for TWP" (CPRHR henceforth) data set [*Comstock et al.*, 2013] provides cloud microphysical properties and heating rate profiles retrieved from ground-based measurements by the millimeter wavelength cloud radar [*Moran et al.*, 1998] and the micropulse lidar [*Spinhirne*, 1993]. This study uses vertical profiles of generalized effective ice particle size (D_{ge}) [*Fu*, 1996], ice water content (IWC), and cloud phase provided in CPRHR. The retrieval method used by CPRHR to determine cloud microphysical properties depends on which of the two instruments detect clouds (radar, lidar, or both). If only radar detects clouds, an empirical relation based on *Hogan et al.* [2006] is used to obtain IWC and D_{ge} from the radar reflectivity. If only lidar detects clouds, the retrieval follows the method outlined by *Heymsfield et al.* [2005]. If both instruments detect clouds,

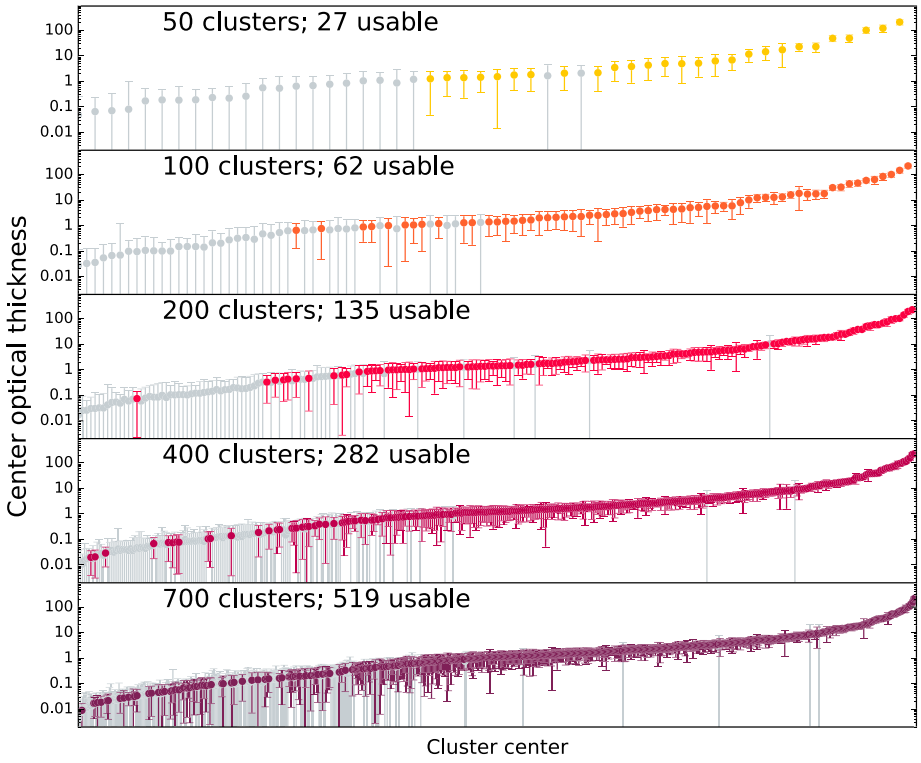

Figure 1. Distribution of cluster center COTs from k = 50, 100, 200, 400, and 700 clusters. Error bars represent the intracluster standard deviation. Gray dots indicate clusters deemed unusable, due to its standard deviation being greater than the center value.

the retrieval algorithm of *Wang and Sassen* [2002] is used. Uncertainties in the CPRHR data set are evaluated in *Comstock et al.* [2013], but it is noted that the analysis conducted here is not sensitive to the accuracy of this input data set. It merely serves to provide a realistic distribution of cloud scenes that spans the range of regimes expected in the tropics.

For the TWP site at Darwin, Australia, the CPRHR covers approximately 6 years from 2005 to 2011. Performing IC analysis on all clouds available is not feasible and redundant, as many clouds may have similar features. To reduce redundancy and provide a tractable set of unique cloud types that span the range of clouds observed in nature, we use the k-means clustering algorithm, which partitions the data into k (user-specified) clusters. The k-means algorithm initializes k centroids, assigns each data point to the closest centroid, and then perturbs the centroid positions to minimize the sum of Euclidean distance between all data points and their respective centroids [*Wilks*, 1997]. For clustering the cloud profiles, we define five features that describe each cloud: mean D_e, mean IWC, cloud top height, T_c, and cloud geometric thickness. The clustering analysis is limited to single-layer ice clouds whose T_c is below 253.15 K; clouds not meeting these criteria are excluded.

The choice of k is based on the criterion that the intracluster spread of COT should be small, so that all clouds in the cluster are well represented by the cluster center. This is to ensure that the channels selected for each cloud type can be associated with its occurrence frequency in the channel selection process. As a simple quantitative test of this requirement, we require that the standard deviation of COT be less than the center value. Figure 1 shows the application of this criterion onto clusters resulting from various choices of k. With relatively smaller numbers of clusters (k = 50, 100, and 200), many clusters have a large standard deviation, and are therefore too broad for our analysis. Furthermore, choosing a smaller k leaves very few thin cloud clusters, which are among the most populous and important ice cloud types. Even at k = 400, clusters with narrow COT ranges remain quite sparse. Through experimentation, it was determined that k = 700 adequately represents the spectrum of ice clouds in the composite ARM TWP data set.

Figure 2 compares the raw data (before clustering) to the clustering result. Before clustering, there were approximately 4.14×10^5 single-layer clouds of ice phase with temperatures below 253.15 K. After clustering,

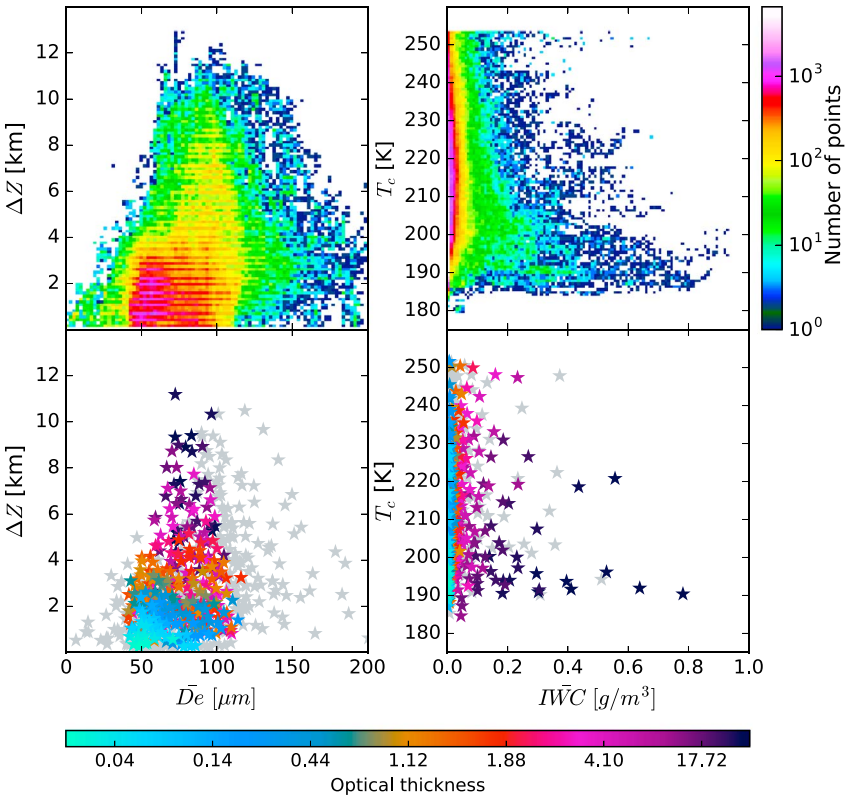

Figure 2. (top row) Density plots of all data before clustering, for geometric thickness versus mean D_e (left) and T_c versus mean IWC (right). (bottom row) Scatterplot of cluster centers; gray stars indicate that the cluster was not used in the simulations due to particle size being outside the valid range of the ice crystal scattering properties. Cluster used in the IC analysis are represented as stars colored by COT.

using $k = 700$, the resulting cluster centers span the complete range of cloud properties present in the raw data set. Due to the limitations of the ice crystal scattering property data set [*Baum et al.*, 2014], which is limited to D_e between 10 and 120 μm, 348 out of the 700 clusters were usable (shown as colored stars in Figure 2, bottom row). The number of clouds included by the 348 clusters is approximately 2.19×10^5. Scatterplots of cluster centers show that the centers cover a dynamic range comparable to the raw data set in every cloud property aside from particle size.

3. Channel Selection Using Information Content

3.1. Radiative Transfer Model

A model based on the Vector Linearized Discrete Ordinate Radiative Transfer model (VLIDORT) [*Spurr*, 2006] is used to simulate radiances and Jacobians. The High-Resolution Transmission Molecular Absorption (HITRAN) [*Rothman et al.*, 2009] database was used for gas attenuation, and the treatment of Rayleigh scattering follows the methodology of *Bodhaine et al.* [1999]. Line-by-line radiances and Jacobians simulated with this model were convolved with AIRS and Aqua MODIS spectral response functions (SRF) in order to simulate the satellite-observed radiances. It is assumed that all simulated AIRS and MODIS radiances are overcast (100% cloud fraction) and that AIRS and MODIS pixel sizes are the same.

Time-collocated temperature and humidity profiles for the CPRHR data set are obtained from the Merged Sounding (MERGESONDE) product [*Troyan*, 2012] also available from ARM. Trace gas profiles come from two sources: Air Force Geophysics Laboratory atmospheric constituent profiles [*Anderson et al.*, 1986] and the Monitoring Atmospheric Composition and Climate (MACC) reanalysis [*Inness et al.*, 2013]. The vertical resolution of input profiles for each simulation was approximately 250 m inside clouds and 1 km outside of clouds for pressure levels below 50 hPa; above 50 hPa, levels are specified at 30, 20, 10, and 1 hPa.

Radiances and Jacobians were simulated over three surface types: ocean, vegetation, and bare soil. The former uses ocean spectral emissivities derived from *Hale and Querry* [1973] and *Sidran* [1981], while the vegetation

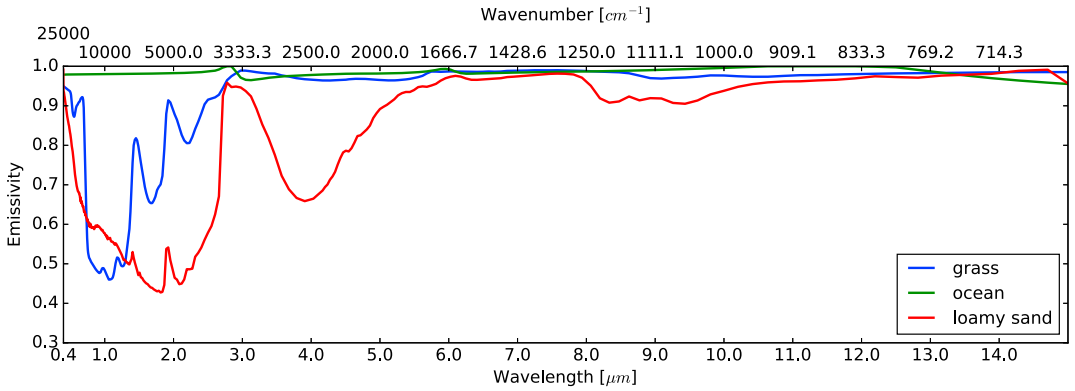

Figure 3. Spectral emissivities of ocean, vegetation (grass), and bare soil (loamy sand).

and bare soil are represented by grass and loamy sand spectral emissivities from the Advanced Spaceborne Thermal Emission Reflection Radiometer spectral library [*Baldridge et al.*, 2009]. Spectral emissivities of these three surface types are shown in Figure 3. All simulations assume daytime conditions with a solar zenith angle of 20°, at seven different viewing angles ±45°, ±30°, ±15°, and 0°, where negative angles indicate that the sensor is on the same side of the Sun.

3.2. Information Content

The information content analysis conducted here is rooted in the concept of Shannon entropy introduced by *Shannon and Weaver* [1949]:

$$S(P) = -\sum_i P(x_i)\log_2 P(x_i). \tag{1}$$

The Shannon entropy (SE) is related to the number of possible states of any random variable. Specifically, the SE in bits is the number of binary digits required to represent the possible range of outcomes. For example, the outcome of a coin can be represented by one bit since there are only two possible outcomes (heads or tails). In this case, the SE would be 1. With two coins, the SE increases to 2, and so on. The concept of SE has been frequently used in remote sensing to quantify the extent to which measurements reduce the SE or, equivalently, the possible solution space of a retrieved variable. This represents a reduction of uncertainty or increased knowledge of the variable, so it is desirable to find measurements that can offer the greatest reduction in SE, i.e., the most IC.

Let the probability density function (PDF) of the cloud property to be retrieved x be $P_0(x)$ and $P_1(x)$ before and after making a measurement, respectively. The IC of the measurement H can be formally defined as the difference in entropy S of the two PDFs:

$$H = S(P_0) - S(P_1). \tag{2}$$

Rodgers [2000] has shown that the multivariate Gaussian distribution for a vector of retrieved variables is

$$S[P(x)] = c + \frac{1}{2}\ln|\mathbf{S_x}| \tag{3}$$

where c is a constant and S_x is the error covariance matrix of the retrieved variables. It follows that the IC of a measurement can be expressed as

$$\begin{aligned} H &= \frac{1}{2}\ln|\mathbf{S_a}| - \frac{1}{2}\ln|\hat{\mathbf{S}}| \\ &= \frac{1}{2}\ln|\mathbf{S_a}\hat{\mathbf{S}}^{-1}|, \end{aligned} \tag{4}$$

where $\mathbf{S_a}$ and $\hat{\mathbf{S}}$ are the prior and posterior error covariance matrices of the retrieved variables, respectively. In our analysis, $\mathbf{S_a}$ is obtained from the climatological standard deviation of the retrieved cloud properties in the ARM TWP data set. Given the Jacobian $\mathbf{K}$ of the measurement with respect to the retrieved variables and the total error covariance of the measurements, $\mathbf{S}_\epsilon$, $\hat{\mathbf{S}}$ can be expressed as

$$\hat{\mathbf{S}} = \left(\mathbf{K}^T\mathbf{S}_\epsilon^{-1}\mathbf{K} + \mathbf{S_a}^{-1}\right)^{-1}, \tag{5}$$

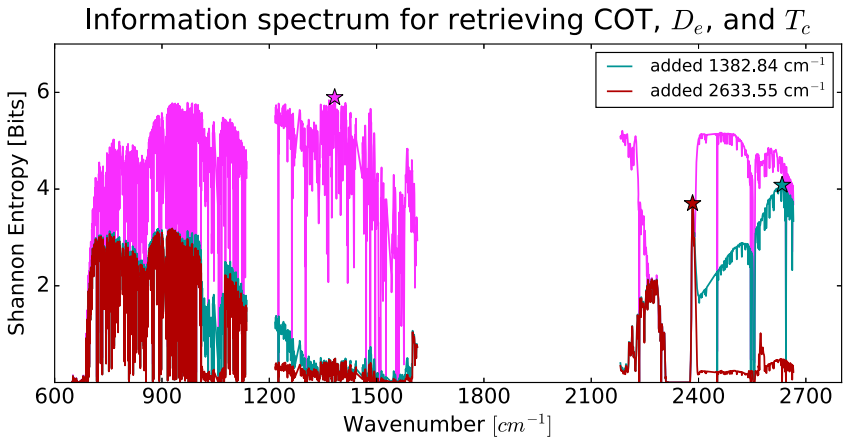

Figure 4. Demonstration of channel selection using IC: AIRS information spectrum before channel selection (magenta), after adding the 936.78 cm^{-1} channel to the a priori error covariance matrix (teal), and after adding both 936.78 cm^{-1} and 2616.38 cm^{-1} channels (maroon). Stars indicate the channel with highest IC during each step.

which is used in equation (4) to calculate the IC of the measurements. We define the Jacobian **K** as

$$\mathbf{K} = \begin{pmatrix} \frac{\partial I_{\nu_1}}{\partial \ln(\mathrm{COT})} & \frac{\partial I_{\nu_1}}{\partial \ln(D_e)} & \frac{\partial I_{\nu_1}}{\partial \ln(T_c)} \\ \frac{\partial I_{\nu_2}}{\partial \ln(\mathrm{COT})} & \frac{\partial I_{\nu_2}}{\partial \ln(D_e)} & \frac{\partial I_{\nu_2}}{\partial \ln(T_c)} \\ \vdots & \vdots & \vdots \\ \frac{\partial I_{\nu_N}}{\partial \ln(\mathrm{COT})} & \frac{\partial I_{\nu_N}}{\partial \ln(D_e)} & \frac{\partial I_{\nu_N}}{\partial \ln(T_c)} \end{pmatrix} \tag{6}$$

where I_{ν_i} is the radiance of channel i at wavelength ν_i, COT is cloud optical thickness, D_e is effective diameter, T_c is cloud top temperature, and N is the total number of channels.

To apply equation (4) to a single channel, we take the row of **K** corresponding to the channel number i, $\mathbf{k_i}$, and assume that the observation error covariance is diagonal, so that each channel has an associated error variance σ_i^{-2}. Then the IC of a single channel can be written as

$$\begin{aligned} H_i &= \frac{1}{2} \ln \left| \mathbf{S_a} \left(\mathbf{k_i}^T \sigma_i^{-2} \mathbf{k_i} + \mathbf{S_a}^{-1} \right) \right| \\ &= \frac{1}{2} \ln \left| \sigma_i^{-2} \mathbf{S_a} \mathbf{k_i}^T \mathbf{k_i} + \mathbf{I} \right|. \end{aligned} \tag{7}$$

We use a sequential selection procedure similar to that described by *Sofieva* [2003] to identify the optimal set of channels for retrieving the properties of each cluster at all seven viewing angles over three surface types. Figure 4 depicts the process graphically. To begin, equation (7) is used to calculate the IC of each channel (shown as the magenta line in Figure 4). When the IC of all channels are determined, we select the channel with highest IC (shown as the magenta star). After this first selection, the selected channel is "added" to the a priori error covariance matrix by

$$\mathbf{S_{a,new}} = \left(\mathbf{k_i}^T \sigma_i^{-2} \mathbf{k_i} + \mathbf{S_a}^{-1} \right)^{-1}. \tag{8}$$

We can now calculate the IC of every channel again (teal line in Figure 4) with respect to the updated a priori error covariance matrix. From the new IC spectrum we can select a channel that yields the most complimentary information to the first. This process is then repeated to select the desired number of channels.

The number of channels to select may be determined from the degree of freedom for signal (DOF), which can be calculated as

$$d_s = tr \left(\left[\tilde{\mathbf{K}}^T \tilde{\mathbf{K}} + \mathbf{I} \right]^{-1} \tilde{\mathbf{K}}^T \tilde{\mathbf{K}} \right), \tag{9}$$

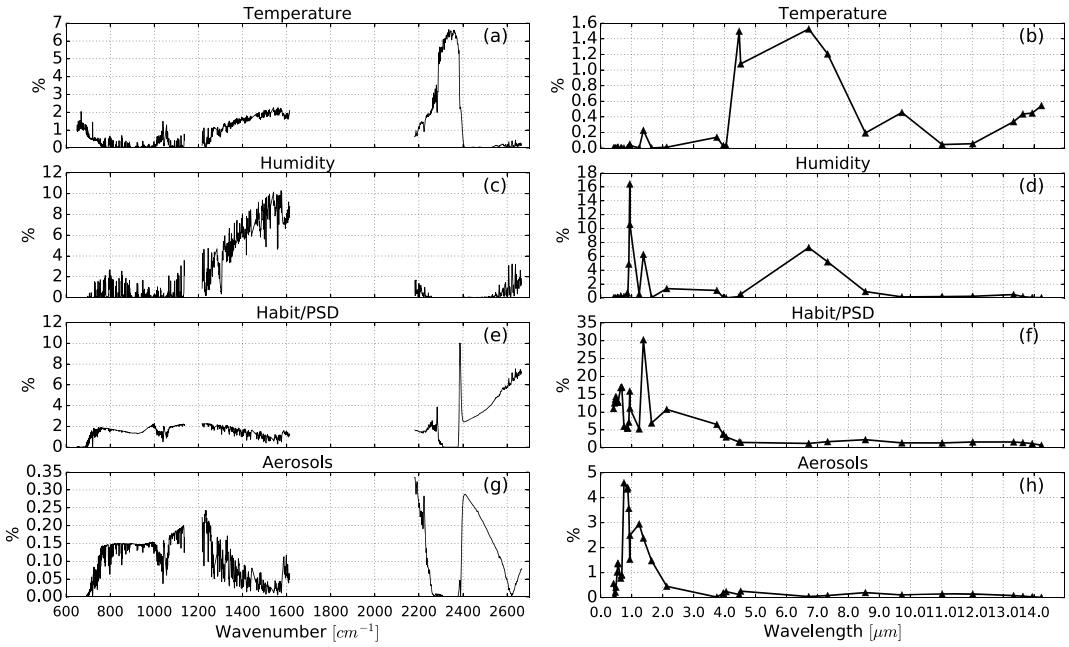

Figure 5. Uncertainty due to the specified source for (a, c, e, and g) AIRS and (b, d, f, and h) MODIS channels. Percentages indicate the magnitude of the error standard deviation relative to the mean radiance of the simulations used to generate each uncertainty.

where $\tilde{\mathbf{K}} = \mathbf{S}_\epsilon^{-\frac{1}{2}}\mathbf{K}\mathbf{S}_\mathbf{a}^{\frac{1}{2}}$. The DOF cannot be larger than the number of retrieved variables, which is three in our case (COT, D_e, T_c). We found that the DOF of most clusters were typically slightly above 2. Since more than two channels are needed to take advantage of a DOF above 2, for each cluster we make three channel selections.

3.3. Uncertainty Sources

Channel selection depends on the uncertainties of each channel [*L'Ecuyer et al.*, 2006], as described by the total error covariance $\mathbf{S}_\epsilon$. This matrix includes the measurement error covariance matrix, which characterizes the uncertainty in the observed radiances, as well as systematic forward modeling uncertainties, i.e., uncertainties in the simulated radiances caused by inherent errors in the parameters used in the forward model. For instance, atmospheric thermodynamic profiles taken from any source, whether they derive from radiosondes, reanalyses, or satellite retrievals, all have associated errors. Radiances forward modeled using these profiles will unavoidably deviate from the actual observations. Uncertainties of this type can be estimated for each input source by randomly perturbing the input profiles and using the resulting radiances to estimate the error covariance matrix. The resulting magnitudes of each forward model uncertainty are summarized as a percentage relative to the mean radiances in Figure 5. Other error sources, such as spatial inhomogeneity and three-dimensional effects, are much harder to estimate and are not treated in this study.

The separate error covariance matrices can be combined as a sum if we assume that all sources are uncorrelated with each other. The total error covariance matrix, which contains all uncertainties, is

$$\mathbf{S}_\epsilon = \mathbf{S}_\mathbf{y} + \mathbf{S}_\mathbf{T} + \mathbf{S}_\mathbf{wv} + \mathbf{S}_\mathbf{habit} + \mathbf{S}_\mathbf{aerosol} \tag{10}$$

where $\mathbf{S}_\mathbf{y}$ is the instrument error covariance matrix, $\mathbf{S}_\mathbf{T}$ represents the uncertainty due to temperature, $\mathbf{S}_\mathbf{wv}$ due to humidity, $\mathbf{S}_\mathbf{habit}$ due to ice crystal assumptions, and $\mathbf{S}_\mathbf{aerosol}$ due to aerosols.

To generate the uncertainties due to temperature, we assume that for every temperature profile, the temperature at each layer is a Gaussian-distributed random variable with an associated standard deviation. It is also assumed that errors in different layers are uncorrelated. We assume that the temperature error standard deviation at each layer is 1.5 K, consistent with documented errors in AIRS temperature profile retrievals at 1 km resolution [*Divakarla et al.*, 2006]. A temperature profile from the MERGESONDE data set at Darwin, Australia was used to generate 600 profiles by randomly sampling temperatures at each layer from the appropriate

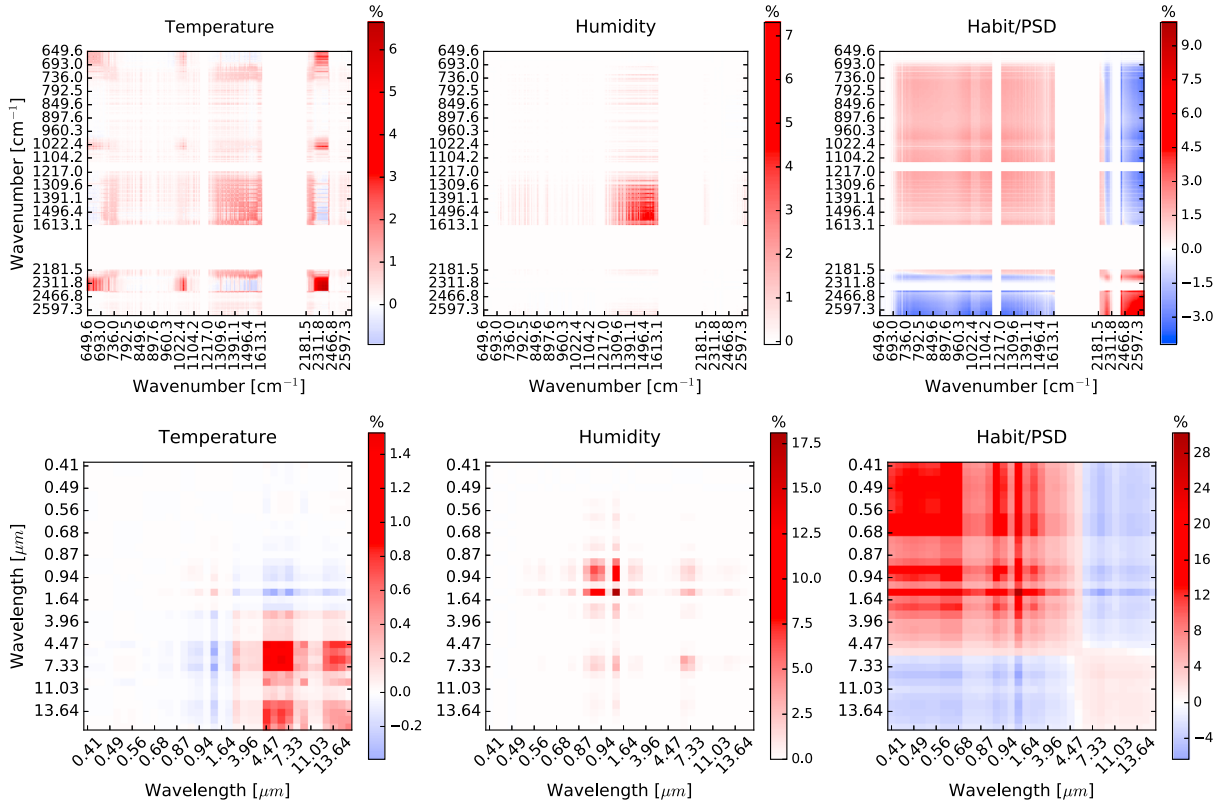

Figure 6. Visualization of (top row) AIRS and (bottom row) MODIS error covariance matrices for temperature, humidity, and assumptions in the ice crystal habit and particle size distribution, calculated using equation (11). In Figure 6 (top row), the white gaps are regions where AIRS does not have channels.

Gaussian distributions. A set of AIRS and MODIS radiances was generated for each of these profiles, and the covariance matrix of the resulting radiances was then used as the error covariance matrix due to temperature profile errors. The error covariance matrix includes off-diagonal elements that represent covariances between errors in different channels.

Figures 5a and 5b show the diagonal elements of this error covariance matrix that represents the uncertainty due to temperature profile errors. Uncertainties due to temperature are typically less than 3% of the mean radiance for most AIRS channels. Temperature uncertainties are highest around 2200–2400 cm^{-1} (4.5–4.2 μm), approaching almost 7% at around 2300 cm^{-1} (4.35 μm). Uncertainties across all MODIS bands are less than 2% with the highest values reaching 1.5% at 4.5 and 6.7 μm (2200 and 1492 cm^{-1}).

The temperature error covariance matrices, together with the others that have off-diagonal elements, are visualized in Figure 6. For ease of interpretation, the matrices are plotted in terms of percentages relative to the mean radiances. Each element is calculated as

$$c_{i,j} = 100 * \begin{cases} \sqrt{\frac{\sigma_{i,j}}{\bar{l}_i \bar{l}_j}} & \sigma_{i,j} \geq 0, \\ -\sqrt{\frac{-\sigma_{i,j}}{\bar{l}_i \bar{l}_j}} & \sigma_{i,j} < 0, \end{cases} \tag{11}$$

where $c_{i,j}$ is the plotted value, $\sigma_{i,j}$ is the (i, j) element in the covariance matrix, and $\bar{l}_i, \bar{l}_j$ are the mean radiances of channel i and j. Plotted this way, the diagonals will have identical values to Figure 5. For the temperature error covariance matrices, covariances are strongest between the region near 2300 cm^{-1} (4.3 μm) and 650 cm^{-1} (15.4 μm).

The diagonals of the error covariance matrix due to uncertainty in the assumed humidity profile were constructed using water vapor Jacobians from the RTM. Given the specific humidity weighting functions

Table 1. List of Habit and PSD Combinations for Obtaining the Habit/PSD Uncertainties

Habit Type	PSD Type	Source of Scattering Properties
General habit mixture	Fit to campaign data [1]	*Baum et al.* [2014]
Solid columns	Fit to campaign data [1]	*Baum et al.* [2014]
Aggregate columns	Fit to campaign data [1]	*Baum et al.* [2014]
Droxtals (lightly roughened)	Exponential	*Yang et al.* [2013]
Droxtals (lightly roughened)	Hansen-Travis Gamma, $b = 0.2$	*Yang et al.* [2013]
Droxtals (lightly roughened)	Hansen-Travis Gamma, $b = 0.4$	*Yang et al.* [2013]
10-element plates (severely roughened)	Exponential	*Yang et al.* [2013]
10-element plates (severely roughened)	Hansen-Travis Gamma, $b = 0.2$	*Yang et al.* [2013]
10-element plates (severely roughened)	Hansen-Travis Gamma, $b = 0.4$	*Yang et al.* [2013]

$\partial I_\nu / \partial \ln q(z_i)$, at each wavelength ν the standard deviation can be calculated using

$$\begin{aligned}\sigma_{q,\nu} &= \sum_i^{N_{\text{layer}}} \frac{\partial I_\nu}{\partial q(z_i)} \left(\frac{\text{UNC}(z_i)}{100\%} q(z_i) \right) \\ &= \sum_i^{N_{\text{layer}}} \frac{\partial I_\nu}{\partial \ln q(z_i)} \left(\frac{\text{UNC}(z_i)}{100\%} \right)\end{aligned} \tag{12}$$

where $\text{UNC}(z_i)$ is the uncertainty in specific humidity in percentage relative to the specific humidity at height z_i. Based on *Divakarla et al.* [2006], the uncertainty in specific humidity was assumed to be 20% at the surface and linearly increases to 50% at 250 hPa. At all altitudes above 250 hpa, the uncertainty was assumed to be 50%. The standard deviations at all wavelengths, calculated by equation (12), make up the diagonal of the error covariance matrix. To obtain the off diagonals, a method similar to the temperature uncertainty is used, where 600 profiles were generated by randomly sampling humidity at each layer using the appropriate standard deviation. The correlation matrix of the radiances were then used to construct the off-diagonal elements of the error covariance matrix.

The relative magnitude of humidity uncertainties are shown in Figures 5c and 5d. As expected, humidity errors induce the largest uncertainty in AIRS channels within the water vapor absorption regions between 1200 and 1600 cm^{-1} (8.3 and 6.3 μm), peaking at around 10%. In the same spectral region, MODIS uncertainties increase to 8%, but the maximum is 16% at 0.9 μm where water vapor has low transmission [*Eldridge*, 1967]. Covariances among channels are localized in the water vapor absorption bands, for example, within 1200 and 1600 cm^{-1} for AIRS (Figure 6). In MODIS channels, these wavelengths have high covariances as well, although the magnitudes are higher in the near-infrared water vapor absorption bands, such as 1.38, 0.94, and 0.91 μm.

Another source of uncertainty is the assumption of ice crystal habit and particle size distribution (PSD). To estimate these uncertainties, 30 different clouds ranging from optically thin (0.009) to thick (7.4) from the clustering analysis were used to simulate radiances. For each cluster, nine different habit and PSD combinations were assumed, as listed in Table 1. The first three habit/PSD types were adopted from *Baum et al.* [2014], where the PSD was based on a collection of in situ campaigns. For the last six types, whose scattering properties are described by *Yang et al.* [2013], an exponential distribution and two different gamma distributions were specified. The gamma distributions are based on equation (2.56) of *Hansen and Travis* [1974]:

$$n(r) = n_0 r^{\frac{1-3b}{3}} e^{\frac{r}{br_e}}. \tag{13}$$

where b is a unitless factor controlling the shape of the distribution. To obtain the covariance matrix, the intracluster mean was first removed from the simulated radiances for every cluster. The resulting radiances can be then interpreted as the perturbations about the mean due to the assumed habit and PSD, resulting in 270 sets of radiance perturbations that define the uncertainty covariance matrix.

As shown in Figures 5e and 5f, uncertainties are under 2% for AIRS channels within 650 cm^{-1} to 1630 cm^{-1} (15.4 to 6.1 μm). Above 2200 cm^{-1} (4.55 μm), the uncertainty becomes significantly higher in many channels, notably at 2390 cm^{-1} (4.2 μm) where the uncertainty peaks at 10%. MODIS channels in the NIR and visible

suffer more notably from this type of uncertainty. Below 4 μm, all uncertainties are above 5%, exceeding 10% in many of the visible bands, with the highest value being 30% at 1.375 μm. The magnitude of these uncertainties is mostly consistent with *Cooper et al.* [2006] who reported that uncertainties of this type are typically less than 5% in the infrared and grow to around 20–30% in the visible. By comparing the habit/PSD error covariance matrices of AIRS and MODIS (Figure 6), it is apparent that habit/PSD errors covariances are more significant in MODIS visible and near-infrared channels.

Since visible and NIR channels are sensitive to aerosols, the presence of aerosols in cloudy scenes should also be considered a source of uncertainty. We estimated this uncertainty by extracting the mean aerosol optical thickness (AOT) in the tropics (20°N, 20°S) during 2007 from the MACC reanalysis for four different aerosol types: sea salt, organic carbon, soot, and sulfate. The sum of these four average AOTs was around 0.14. These AOTs were distributed vertically by assuming an exponential distribution with an *e*-folding height of 3 km. The mean radiance perturbation due to aerosols over all clusters were assumed to be the standard deviations for the diagonal of the aerosol error covariance matrix. Aerosol uncertainties in AIRS channels are less than 0.5% in all channels. Aerosols have a much more prominent effect on MODIS radiances, peaking at around 4.5% at the 0.74 μm band. One source of aerosol that we have not included is dust, which can be a major source of aerosols in North Africa and the Middle East. However, the AOT value used here (0.14) should be representative of the mean AOT in the tropics outside of these areas [*Hsu et al.*, 2012]. As such, the aerosol uncertainty used in this study should be adequate for most scenarios, and the addition of dust is unlikely to significantly impact the magnitude and spectral characteristics of aerosol uncertainty.

The instrument uncertainty matrix $\mathbf{S}_y$ is assumed to be diagonal. The error variances of MODIS solar reflective bands were derived using the instrument signal-to-noise ratio provided by *Xiong et al.* [2003a], and the error variances of MODIS thermal bands were derived from nedT values from *Xiong et al.* [2003b]. Error variances of AIRS channels were derived using the nedT values provided in the channel property files available at https://disc.gsfc.nasa.gov/AIRS/documentation/v6_docs/v6releasedocs-1/v6-chan-prop-files.zip.

4. Optimal Channels for Ice Cloud Retrievals

Using the IC approach, we select optimal channels for retrieving COT, D_e, and, T_c. All three parameters are fundamental to the radiative characteristics, as COT and D_e controls the scattering and absorption characteristics of the cloud, and T_c is an indicator of outgoing longwave radiation. The channel selection process described in the previous section was carried out for every cluster, over all viewing angles, over three surfaces types: ocean, vegetation, and bare soil.

4.1. Stand-Alone AIRS Retrievals

Results from simulations over ocean are presented as a baseline, since retrievals over ocean are less problematic than over land surfaces. Figure 7 shows the number of times that AIRS channels in each 5 cm^{-1} spectral bin are selected from all retrieval simulations over an oceanic surface. The results clearly identify a small subset of preferred spectral ranges for AIRS ice cloud retrievals around 930, 2400, and 2630 cm^{-1} (10.75, 4.17, and 3.80 μm). These regions contain the most information overall, independent of COT, but some channels around 700 cm^{-1} (14.3 μm) become important for retrieving thinner clouds. The IC selections favored CO_2 slicing channels near 2400 cm^{-1} (4.2 μm) in the shortwave infrared (SWIR) over the midinfrared channels around 700 cm^{-1}. Although in the SWIR region (2380 to 2600 cm^{-1}) the uncertainties due to habit/PSD are higher than those at other wavelengths, there is less absorption from other gases that could increase uncertainties at longer wavelengths causing retrievals to favor the SWIR.

It is known that the usage of SWIR radiances includes some complications, such as solar contamination and non-LTE effects. However, the AIRS version 6 temperature retrieval has experienced improvement in temperature retrievals over version 5 after including and appropriately preprocessing SWIR channels [*Susskind et al.*, 2014]. Given that temperature sounding retrievals have benefited from the addition of SWIR channels, it is plausible that these channels can potentially improve cloud temperature retrievals as well.

The order in which the channels were selected is also shown in Figure 7, indicating the relative importance of each spectral region. CO_2 slicing channels were rarely selected first; most of the first selections occurred in the 2600 and 930 cm^{-1} (3.8 and 10.8 μm) regions, which suggests that overall the AIRS measurements carry more information for COT and D_e than T_c. To verify this, a singular value decomposition (SVD) is applied to $\tilde{\mathbf{K}}$, revealing why each channel is selected.

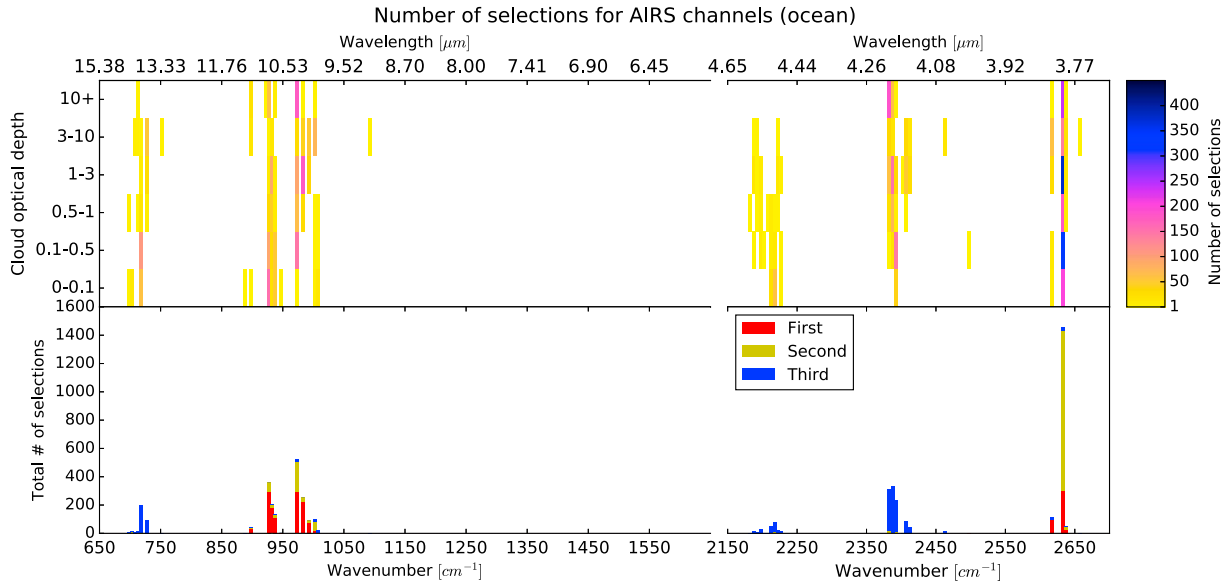

Figure 7. (top) Number of AIRS channel selections within each 5 cm^{-1} bin for ocean surface simulations, over all clusters and all viewing angles, categorized by COT. (bottom) Total number of AIRS channel selections within each 5 cm^{-1} bin.

Analysis of

$$\tilde{\mathbf{K}} = \mathbf{S}_{\epsilon}^{-\frac{1}{2}} \mathbf{K} \mathbf{S}_{\mathbf{a}}^{\frac{1}{2}} \tag{14}$$

is valuable because it determines the effective rank of the problem [*Rodgers*, 2000]. SVD is similar to eigenvalue decomposition but can also be applied to nonsquare matrices such as $\tilde{\mathbf{K}}$. SVD decomposes a matrix into a set of singular values and singular vectors. In this application, the singular values give a relative estimate of precision, while the singular vectors indicate which retrieved variables are being measured. Also, since the singular vectors are orthogonal, SVD can show whether retrieved variables can be measured independently. For this reason, using SVD to decompose $\tilde{\mathbf{K}}$ reveals what spectral regions were most impactful toward retrieving COT, D_e, or T_c. In conjunction with the IC channel selection, SVD gives insight into why the channels were selected and which variables the select channels help retrieve. Singular value decomposition of the matrix $\tilde{\mathbf{K}}$ can be expressed as

$$\tilde{\mathbf{K}} = \mathbf{U} \mathbf{\Lambda} \mathbf{V}^{\mathbf{T}}. \tag{15}$$

Each column vector of $\mathbf{U}$ is the basis in the measurement space and can be interpreted to be "measuring" the retrieved variables as indicated by the corresponding singular vectors (column vectors of $\mathbf{V}$). The singular values in $\mathbf{\Lambda}$ represent the weighting of the corresponding basis [*Rodgers*, 2000]. Figure 8 shows an example of SVD applied to a cloud with COT of about 1.36. The highest weighted singular vector (first column of $\mathbf{V}$) shows highest magnitudes for COT and then D_e, indicating that the corresponding measurement basis contributes most to these two variables, while its contribution to T_c is much smaller. It is expected that the channels with highest values in the most heavily weighted basis were the ones picked first in the channel selection process.

In most cases, the singular vectors do not point to just one retrieval variable, making it hard to interpret which channels impact each variable. However, since the singular vectors are orthogonal, it is possible to apply transformations so that the singular vectors point to one retrieval variable only. Let $\vec{v}_1, \vec{v}_2, \vec{v}_3$ be the column vectors of $\mathbf{V}$ so that $\mathbf{V} = [\vec{v}_1\ \vec{v}_2\ \vec{v}_3]$. We would like to find coefficients $\vec{c} = [c_1\ c_2\ c_3]$ such that

$$c_1\vec{v}_1 + c_2\vec{v}_2 + c_3\vec{v}_3 = \begin{bmatrix} 1 \\ 0 \\ 0 \end{bmatrix} \text{or} \begin{bmatrix} 0 \\ 1 \\ 0 \end{bmatrix} \text{or} \begin{bmatrix} 0 \\ 0 \\ 1 \end{bmatrix}, \tag{16}$$

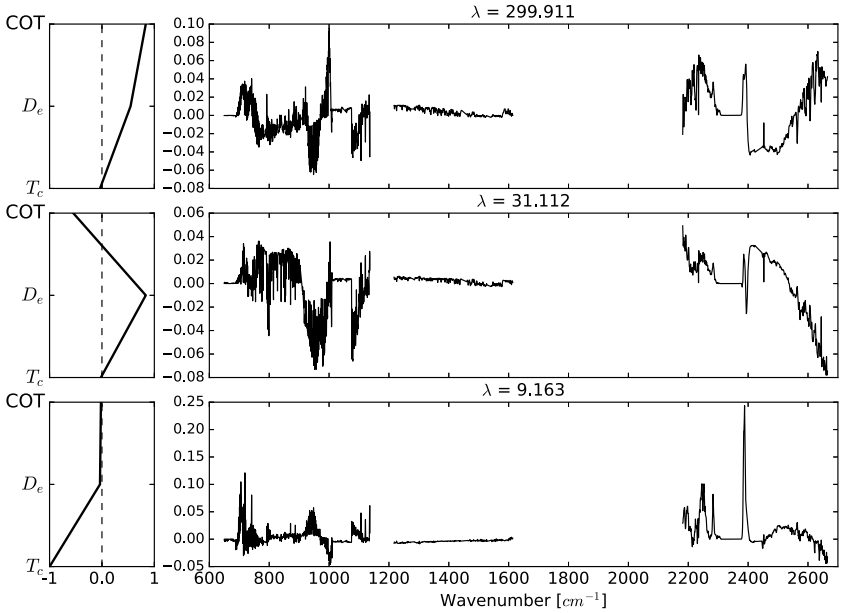

Figure 8. (left column) Singular vectors and (right column) their corresponding basis in measurement space for a cloud with a COT of 1.36. The singular vectors indicate which retrieved variables the measurement bases help constrain. In the top row, for instance, since the singular vector value for T_c is near zero, the measurement basis on the right does not help retrieve T_c but rather contribute most to COT and then, to a lesser magnitude, to D_e. The values shown on the top part are the singular value from $\mathbf{\Lambda}$ of equation (15).

where the vector $[1\ 0\ 0]^T$ represents a singular vector with a nonzero component only in the direction of COT, $[0\ 1\ 0]^T$ one with nonzero component only for D_e, and so on. Equivalently,

$$\mathbf{V}\vec{c} = \begin{bmatrix}1\\0\\0\end{bmatrix} \text{or} \begin{bmatrix}0\\1\\0\end{bmatrix} \text{or} \begin{bmatrix}0\\0\\1\end{bmatrix}. \tag{17}$$

Then $\vec{c}$ can be solved by

$$\vec{c} = \mathbf{V^{-1}} * \left(\begin{bmatrix}1\\0\\0\end{bmatrix} \text{or} \begin{bmatrix}0\\1\\0\end{bmatrix} \text{or} \begin{bmatrix}0\\0\\1\end{bmatrix} \right). \tag{18}$$

By multiplying $\vec{c}$ onto $\mathbf{U}$, we get $\vec{u'} = \mathbf{U}\vec{c}$, where $\vec{u'}$ is a measurement basis that corresponds to a singular vector of $[1\ 0\ 0]^T$ or $[0\ 1\ 0]^T$ or $[0\ 0\ 1]^T$. The measurement basis $\vec{u'}$ isolates each individual retrieval variable. The weightings (singular values) of each transformed basis may be also calculated by

$$\lambda' = |c_1|\lambda_1 + |c_2|\lambda_2 + |c_3|\lambda_3, \tag{19}$$

where λ_1, λ_2, and λ_3 are the singular values (diagonal elements of $\mathbf{V}$) corresponding to the untransformed bases. Figure 9 shows the result of applying the transformation onto the vectors of Figure 8. After this transformation, it is now seen that, for this particular cloud, channels near 2600 cm^{-1} (3.85 μm) primarily constrain COT. Also, the transformed basis corresponding to COT and D_e have higher weights relative to that of T_c, indicating that the channel constraining T_c is likely to have been selected last.

Using the weights calculated from equation (19), the weighted average of measurement bases over all clusters and viewing angles were calculated, as shown in Figure 10. The average bases of AIRS for D_e and T_c both have high magnitudes in the SWIR, explaining the tendency of IC to select channels in this spectral region. In particular, the peak near 2640 cm^{-1} (3.79 μm) coincides with the most selected channel in Figure 7. Highest values in the average AIRS basis for COT occur in the window region near 1000 cm^{-1} (10 μm). In the AIRS basis for D_e, channels throughout the 800–1000 cm^{-1} (12.5-10 μm) have peak magnitudes of around 0.02,

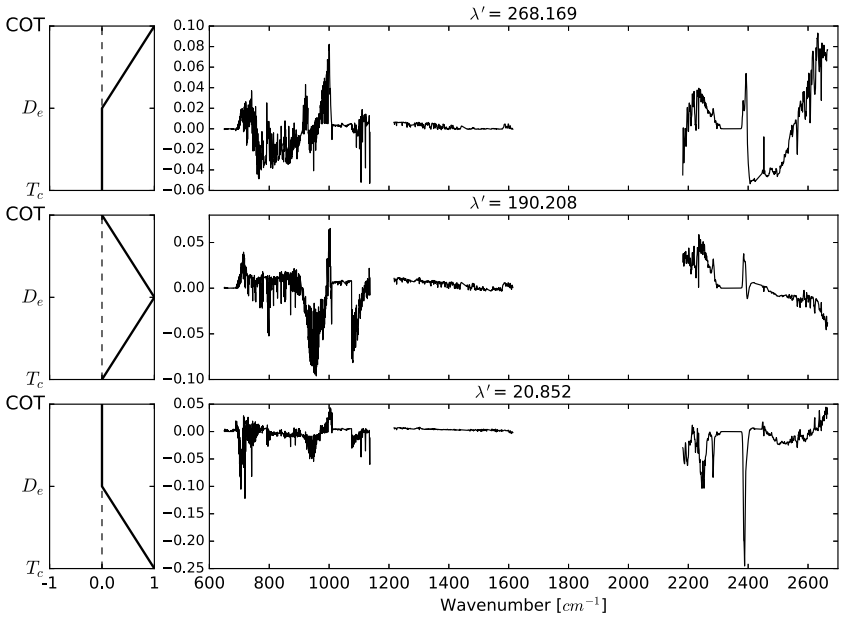

Figure 9. (left column) Transformed singular vectors and (right column) their corresponding measurement basis after applying the transformation of equation (18) onto the same cloud as used in Figure 8. After the transformation, the singular vectors point only to one retrieval variable, and the measurement basis can be interpreted to be contributing to one variable only.

while the largest magnitude (−0.07) occurs around 2640 cm^{-1} (3.79 μm). This indicates that although the window channels are potent for retrieving D_e, the SWIR channels may be a better alternative. Another feature of the AIRS D_e basis is that the thin cloud basis overall has larger magnitudes than the thick cloud basis, implying that most AIRS channels perform better for retrieving D_e of thinner clouds. The average AIRS basis for temperature has peaks at 700, 1000, 2200, 2245, 2380, 2630, and 2660 cm^{-1} (14.3, 10, 4.55, 4.45, 4.2, 3.80, and 3.76 μm). The spectral regions near 700, 2200, 2245, and 2380 cm^{-1} corresponds to the frequent third channel selections in Figure 7, which confirms that these channels were selected for their sensitivity to temperature.

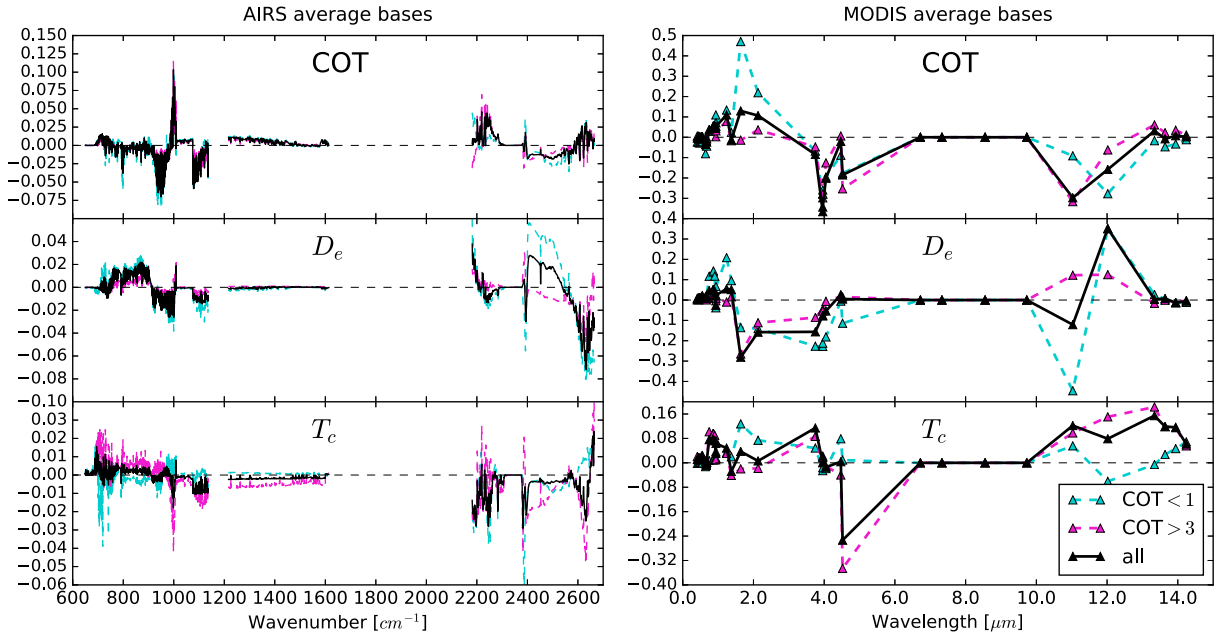

Figure 10. Weighted average of (left column) AIRS and (right column) MODIS measurement bases corresponding to (top row) COT,(middle row) D_e, and (bottom row) T_c, for thin clouds (cyan), thick clouds (magenta), and all clouds (black).

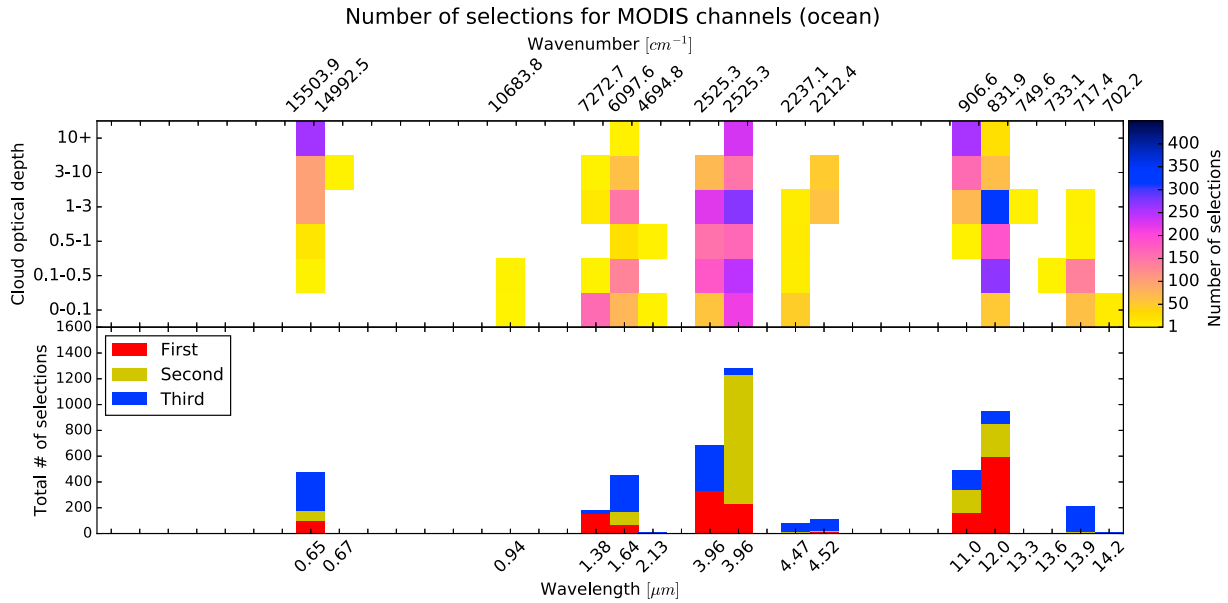

Figure 11. (top) Number of MODIS band selections for ocean surface simulations, over all clusters and all viewing angles, categorized by COT. (bottom) Total number of MODIS band selections. Note that MODIS has two channels, channels 21 and 22, with center wavelengths at 3.96 μm.

Differences between thin and thick clouds are also evident in the bases. The AIRS temperature basis for thin clouds has larger magnitudes near 700 and 2400 cm^{-1}, while the thick clouds basis has peaks at 1000 and 2600 cm^{-1} which are windows channels.

4.2. Stand-Alone MODIS Retrievals

MODIS selections were also performed over ocean, as shown in Figure 11. In contrast with AIRS results, the selected MODIS channels exhibit clear dependence on COT. For instance, the 0.65 μm channel is increasingly favored as COT increases; the 1.38 μm channel is selected only for very thin clouds; the 13.9 μm (720 cm^{-1}) channel was most selected for optically thin clouds while the 11.0 μm (909 cm^{-1}) is selected more as COT increases. The most frequently selected MODIS channel, 3.96 μm (2525.3 cm^{-1}), however, is independent of COT, like the most selected AIRS channels. Note that MODIS has two channels, channels 21 and 22, centered at 3.96 μm. Since the latter obtained more selections, all subsequent mentions of the 3.96 μm channel is meant to refer to channel 22. The second most popular MODIS channel, 12 μm (833 cm^{-1}) is generally selected for clouds with a COT between 0.1 and 3. These results generally agree with the current understanding on sensitivity of these bands to cloud properties. For instance, 1.38 μm has been used for cirrus detection [*Gao et al.*, 1993], the 1.64 and 3.96 μm channels have been shown to be sensitive to particle size [*Lensky and Rosenfeld*, 2008], and the 0.65 μm is a nonconservative band often used in Nakajima-King-type retrievals [*Nakajima and King*, 1990].

Revisiting the SVD results in Figure 10, the average bases of MODIS also explain the channel selections made in Figure 11. The three most selected MODIS channels, which are 3.96, 12, and 11 μm, have large values in the average SVD basis for COT and D_e. The 3.96 μm channel contributes to both COT and D_e, while 11 μm channel contributes mostly to COT and 12 μm channel mostly to D_e. In the basis for D_e, 1.64 μm also stands out, indicating the band's utility for retrieving particle size. Finally, the average basis for T_c, having high values at 4.5 and 13.3 μm, peaks near 4.5 μm, showing why IC analysis favors SWIR channels for temperature retrieval, a result similar to the AIRS selections. Also, similar to the AIRS selections, we found that temperature retrieval channels were rarely selected in the first iteration (Figure 11).

4.3. Surface and Viewing Angle Dependence

Equivalent results for both AIRS and MODIS retrievals over a grass surface are presented in Figures 12 and 13. Overall, the differences between selections over grass and ocean are very subtle, suggesting that the spectral reflectance differences between these two surface types did not alter the IC significantly. Differences in the AIRS selections between the two surfaces were negligible, while for MODIS, the only notable change is that over vegetation there are fewer selections at 0.65 and 1.64 μm, and more frequent selections at 4.52 μm.

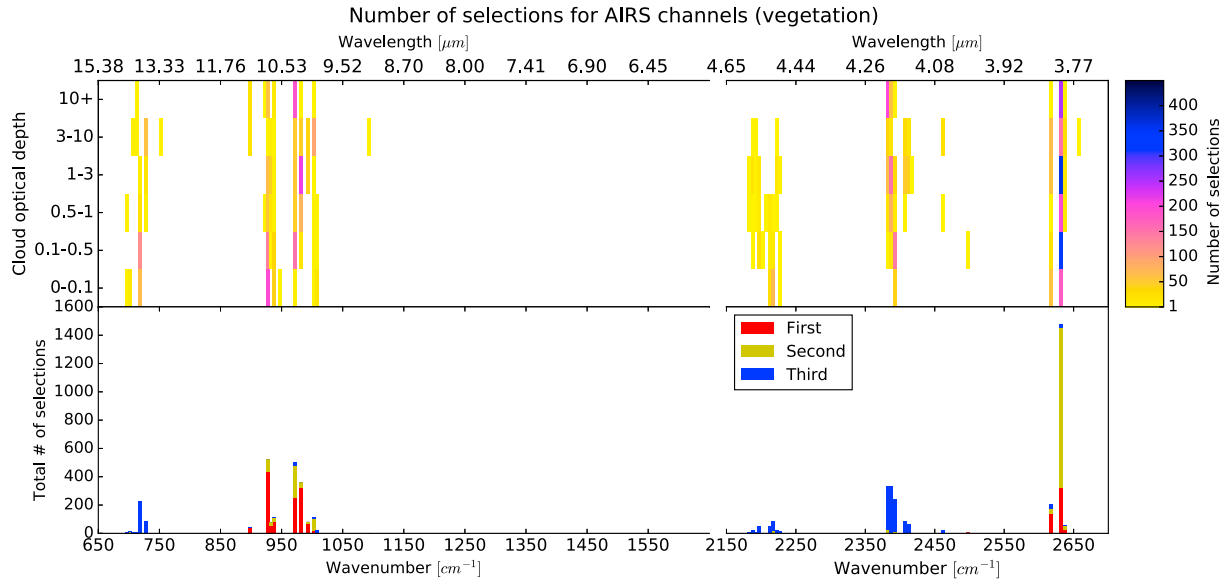

Figure 12. Same as Figure 7, except over grass.

The loss of 1.64 μm channels may be due to the stronger reflectivity of grass in this region (Figure 3). Overall, as both AIRS and MODIS analyses over vegetation were largely similar to the ocean case, we conclude that there is no need to consider separate channel sets over these two surfaces.

Simulations over bare soil, however, results in some notable differences relative to ocean and vegetation. For AIRS (Figure 14), the 2620 cm^{-1} (3.82 μm) channel is almost always selected first over bare soil as opposed to over grass and ocean where the window region near 1000 cm^{-1} (10 μm) is preferred. Second, while selections over grass and ocean favored channels near 2640 cm^{-1} (3.79 μm), retrievals over bare soil favor slightly longer wavelengths at 2620 cm^{-1} (3.82 μm) and channels near 2640 cm^{-1} were selected mostly for thicker clouds. Despite these differences in the selection process, the spectral distribution of the optimal AIRS channels remains largely similar to the two previous surfaces.

In the case of MODIS (Figure 15), IC analysis over bare soil yielded results similar to the grass simulations, where 0.65 and 1.64 μm have fewer selections compared to over ocean, and infrared channels such as 4.52 μm were

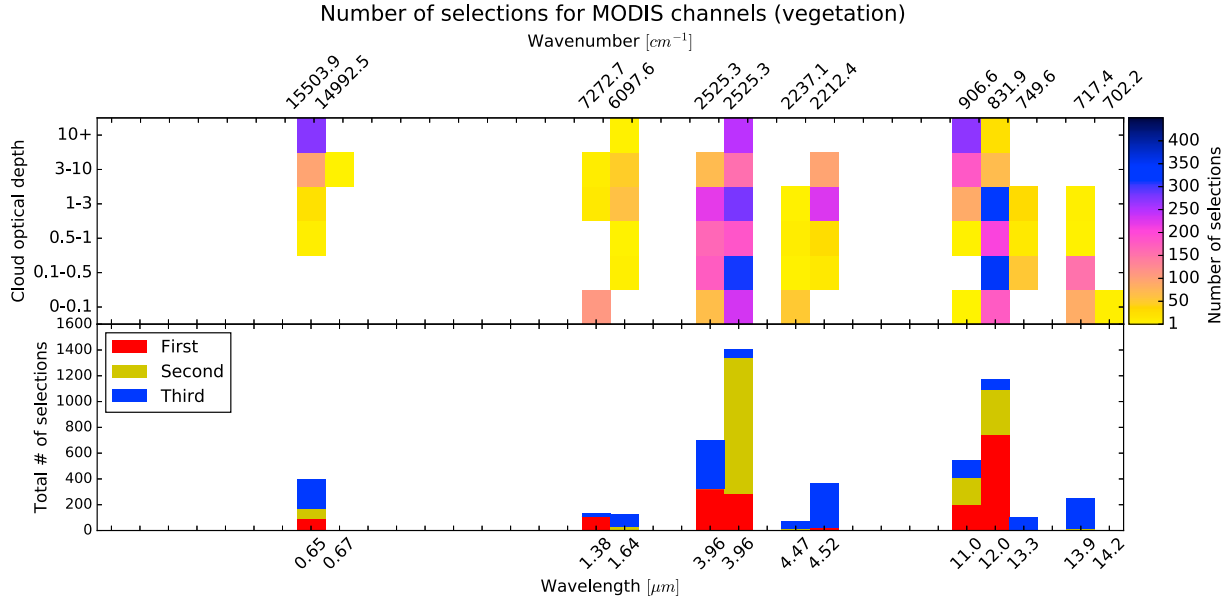

Figure 13. Same as Figure 11, except over grass.

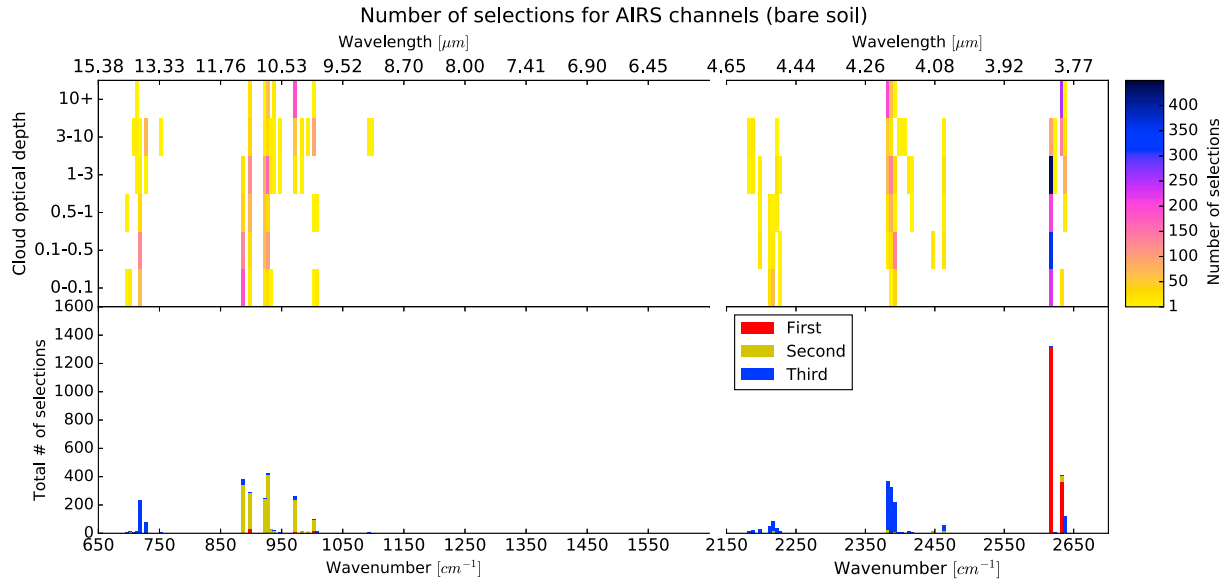

Figure 14. Same as Figure 7, except over bare soil.

favored slightly more. Again, no new channels appeared in the bare soil selections, implying that one set of channels is suitable for both AIRS and MODIS retrievals over most of the tropical region.

Finally, we found that differences due to varying viewing angles were largely negligible in both AIRS and MODIS selections. The only notable difference is that in MODIS selections over bare soil, the 0.65 μm channel is selected more frequently at the expense of the 4.52 μm channel when viewed at 45° off nadir.

4.4. Combined AIRS+MODIS Retrievals

By virtue of their distinct spectral coverage and spectral resolution, there is good reason to expect that AIRS and MODIS may provide complementary information for improved cloud property retrievals. Since these sensors are both on board the Aqua satellite, their spatially and temporally colocated observations are suitable for a joint retrieval. Here we perform channel selection assuming that both AIRS and MODIS channels are available to retrieve an observed cloud. In practice, such a retrieval will be complicated by differences in the

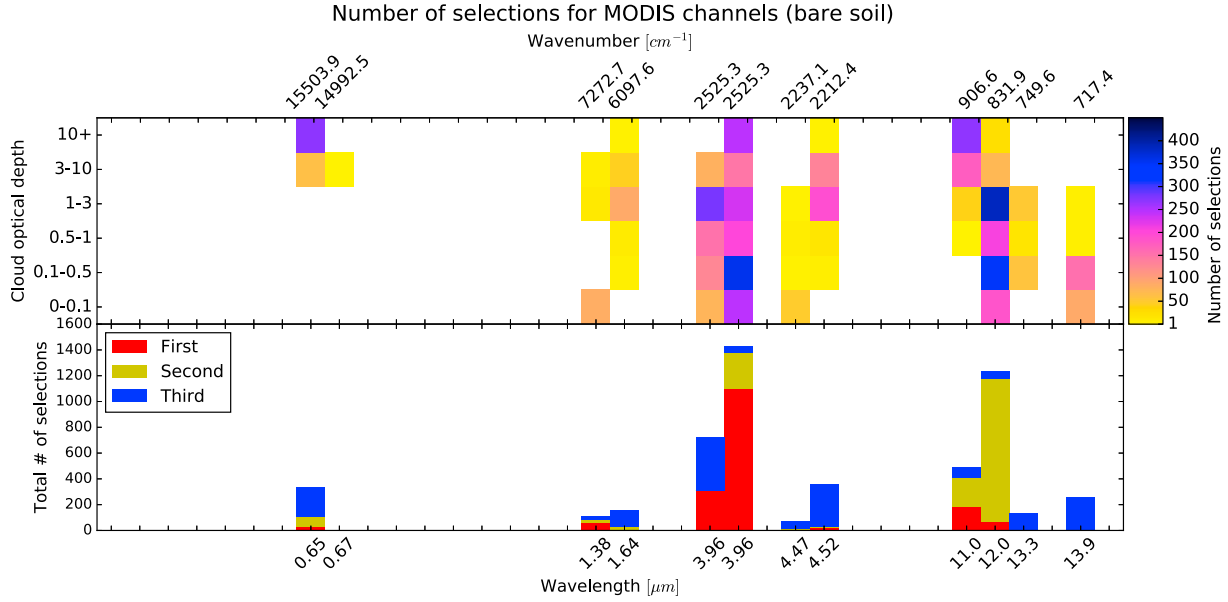

Figure 15. Same as Figure 11, except over bare soil.

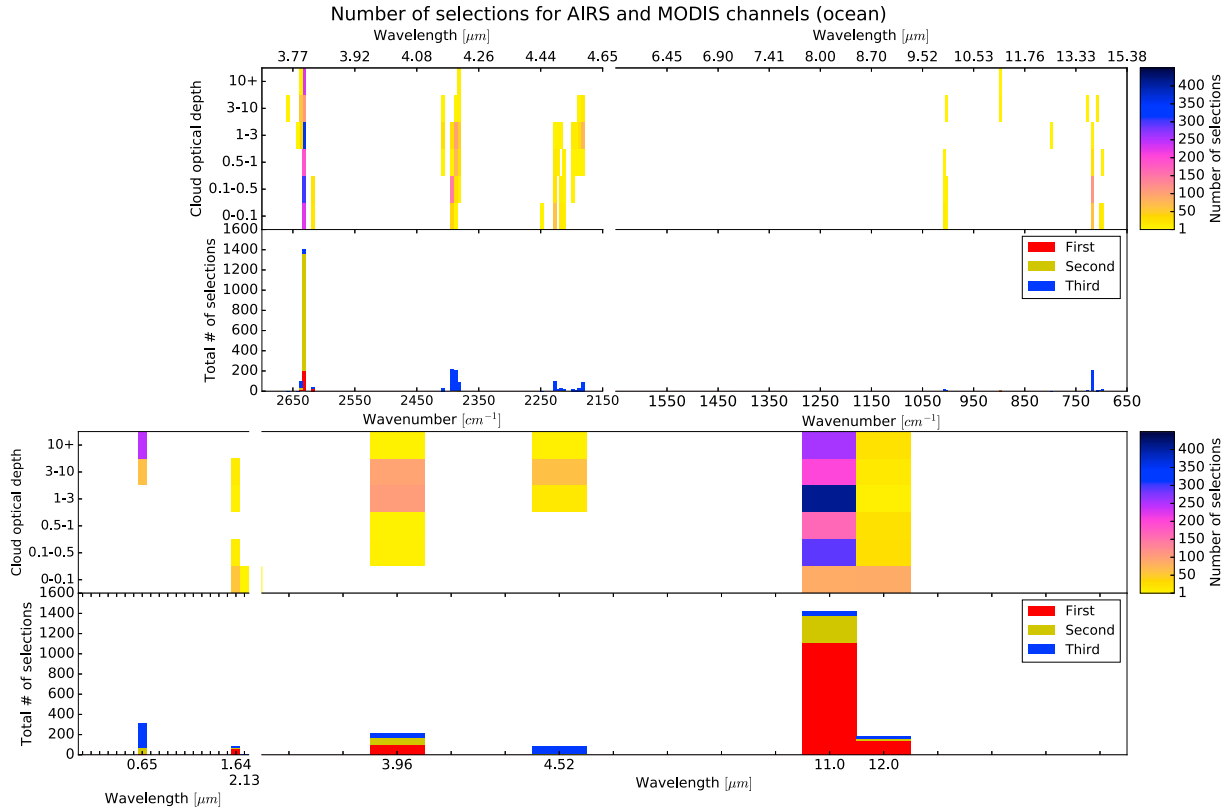

Figure 16. Number of channel selections when simultaneously selecting from AIRS and MODIS for ocean surface simulations. (top plot) The number of AIRS selections in 5 cm^{-1} bins and (bottom plot) the number of selection for each MODIS channel. Note that the wave number axis of Figure 16 (top plot) has been reversed to facilitate comparison between AIRS and MODIS.

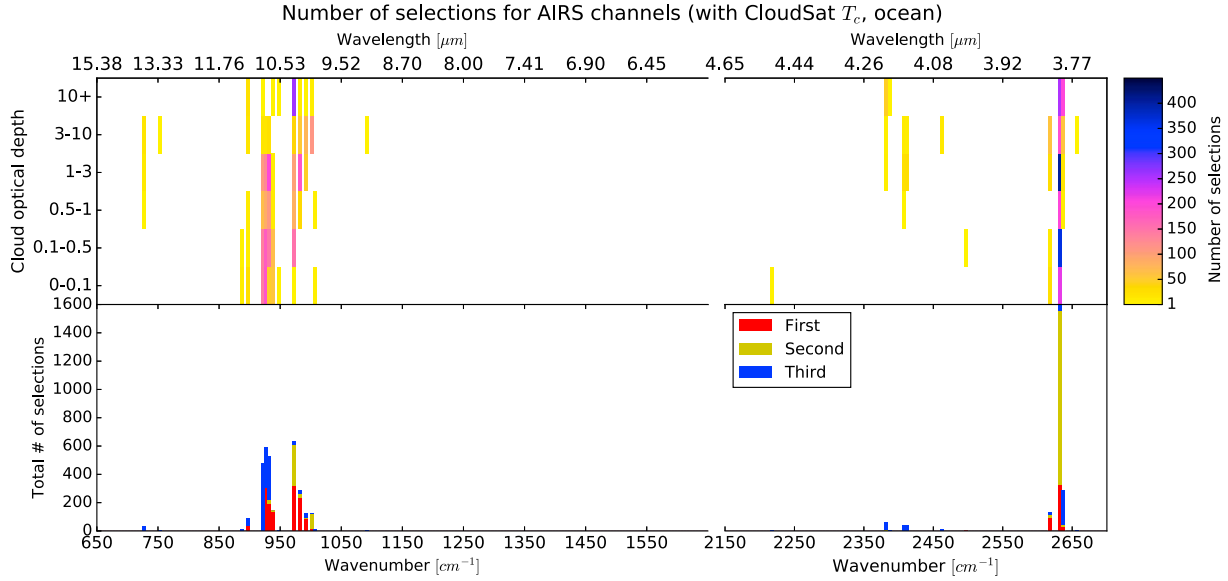

Figure 17. AIR channel selection over ocean assuming a temperature a priori standard deviation of 2K.

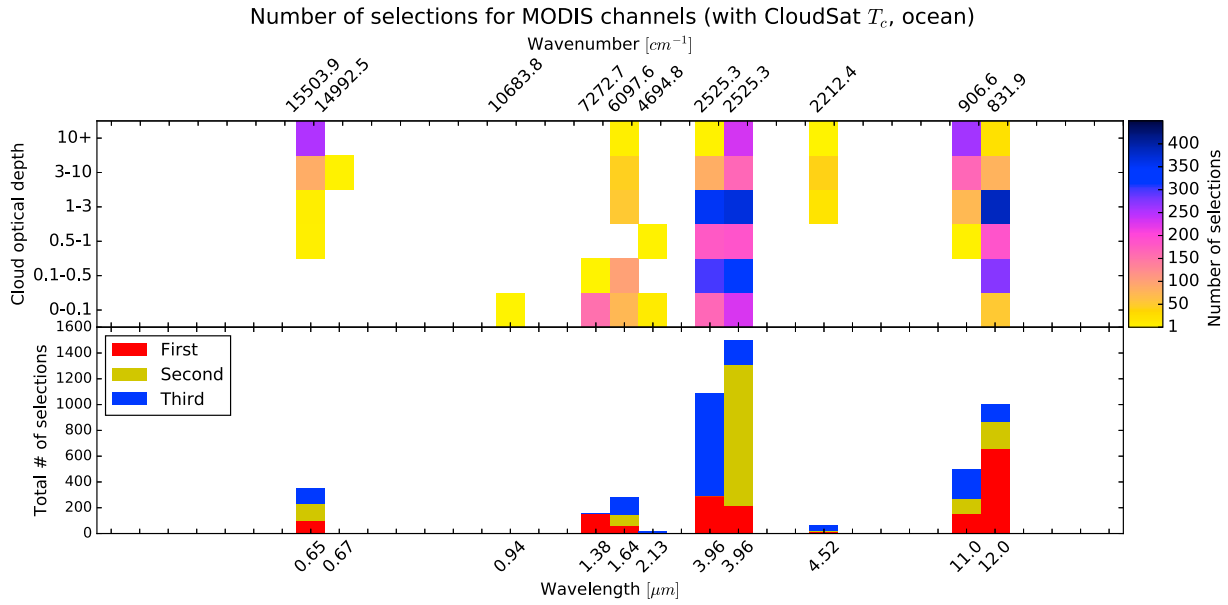

Figure 18. MODIS channel selection over ocean assuming a temperature a priori standard deviation of 2K.

AIRS and MODIS fields of view, but for simplicity here we assume that the observed cloud is spatially homogeneous to facilitate the IC analysis.

Optimal channels for combined AIRS+MODIS ice cloud retrievals over ocean are shown in Figure 16. Both AIRS and MODIS channels were selected, the latter being selected first more often, especially at 11 and 12 μm (909 and 833 cm^{-1}). MODIS longwave window channels were favored over the equivalent AIRS channels, but the AIRS SWIR channels near 2640 cm^{-1} (3.79 μm) outnumber those of MODIS. Of the channels that were previously found to contribute to T_c in Figure 10, which are the 4.47 and 4.52 μm (2237 and 2212 cm^{-1}) MODIS channels and the AIRS channels near 2200 and 2400 cm^{-1} (4.6 and 4.2 μm), AIRS are selected more often. This is expected as the finer resolution of AIRS channels can vertically locate the cloud more accurately. Finally, among the visible and NIR MODIS channels, the 0.65 and 1.64 μm are chosen for combined retrievals with the former being selected frequently for thick clouds. From these results and the previous SVD analysis, it can be concluded that in a combined retrieval, most of the COT and D_e information will come from MODIS, while T_c will almost exclusively be constrained by AIRS.

4.5. Combined Active+Passive Retrievals

As suggested by *Cooper et al.* [2003], there is incentive to combine active and passive observations for cloud retrievals because large cloud boundary uncertainties can induce large biases in COT and D_e retrievals particularly for thin clouds. Active sensors provide the capability to significantly reduce the uncertainty in cloud top heights. The CloudSat Cloud Profiling Radar (CPR) [*Stephens et al.*, 2008] has a vertical resolution of 240 m, which roughly corresponds to a T_c retrieval error of 2 K. To assess IC channel selection while having accurate cloud top boundary, we adopt the methodology of *Cooper et al.* [2006], where the T_c error standard deviation is reduced to simulate the presence of accurate cloud boundary information. We assume the a priori error standard deviation in T_c to be 2 K instead of the 16.2 K (derived from the ARM data set) assumed in the previous analyses and perform the channel selection process as outlined in section 3.

Having accurate a priori cloud boundary significantly influences the channel selection, as can be seen in Figures 17 and 18. All channels sensitive to cloud height, such as the CO_2 slicing channels, are now scarcely selected. Instead, channels previously not selected, such as the AIRS channels near 920 cm^{-1} (10.9 μm) and 2640 cm^{-1} (3.8 μm) now frequently become the third channel, with the latter primarily selected for thicker clouds. No new MODIS channels are selected and most temperature-related channels shift to the 3.96 channel as the third selection. This shows that more accurate a priori cloud boundary can help extract additional COT and D_e information from extra channels especially for AIRS.

Table 2. Channel Sets Obtained From IC Channel Selection, Weighted by Cloud Cluster Populations[a]

	AIRS Stand-Alone			AIRS+MODIS			AIRS+Active	
	cm^{-1} (μm)	Relative Weight		cm^{-1} (μm)	Relative Weight		cm^{-1} (μm)	Relative Weight
1	2633.55 (3.80)	1.000	1	2633.55 (3.80)	1.000	1	2633.55 (3.80)	1.000
2	928.59 (10.77)	0.312	2	11.03 μm (MODIS)	0.937	2	928.59 (10.77)	0.425
3	972.67 (10.28)	0.261	3	719.17 (13.90)	0.181	3	930.07 (10.75)	0.401
4	2391.09 (4.18)	0.211	4	2391.09 (4.18)	0.144	4	923.46 (10.83)	0.325
5	719.17 (13.90)	0.189	5	2388.15 (4.19)	0.139	5	972.67 (10.28)	0.247
6	984.50 (10.16)	0.182	6	12.02 μm (MODIS)	0.129	6	984.50 (10.16)	0.153
7	2388.15 (4.19)	0.180	7	3.96 μm (MODIS)	0.102	7	936.78 (10.67)	0.136
8	936.78 (10.67)	0.162	8	2390.11 (4.18)	0.089	8	971.46 (10.29)	0.104
9	930.07 (10.75)	0.159	9	0.65 μm (MODIS)	0.085	9	2636.79 (3.79)	0.080
10	2616.38 (3.82)	0.113	10	2229.59 (4.49)	0.075	10	2616.38 (3.82)	0.056
11	2384.25 (4.19)	0.078	11	1.64 μm (MODIS))	0.067	11	899.62 (11.12)	0.049
12	971.46 (10.29)	0.077	12	2183.31 (4.58)	0.061	12	994.56 (10.05)	0.045
13	2636.79 (3.79)	0.071	13	2384.25 (4.19)	0.054	13	1000.96 (9.99)	0.031
14	2215.50 (4.51)	0.063	14	2636.79 (3.79)	0.040	14	729.266 (13.71)	0.015
15	2214.57 (4.52)	0.051	15	2616.38 (3.82)	0.031	15	2383.280 (4.20)	0.014

[a]Leftmost column denotes channel selection and weights for stand-alone AIRS retrievals; middle column denotes selection and weights for combined AIRS-MODIS retrievals; rightmost column is for retrievals combining active sensors and AIRS. The weights are relative to the highest weighted channel in each category, so that the channel with highest weight has a relative weight of unity. Only the first 15 highest weighted channels are shown. Channels colored green indicate weights favoring thin clouds (COT < 1), blue indicates those favoring clouds with 1 < COT < 3, and orange indicates those favoring thick clouds (COT > 3).

5. Conclusion

This study applied an objective channel selection methodology utilizing IC to iteratively select optimal channels with the most IC, for tropical ice cloud retrievals under a range of conditions. The complete range of ice cloud types sampled in multiple years at the ARM TWP site is used to extract a set of cloud clusters expected to represent the full dynamic range of optical thickness, effective diameter, cloud top height, and geometric thickness in the tropics. This ensures that the selected channels will be appropriate for most ice clouds found in the tropics. While issues due to cloud inhomogeneity are important in actual retrievals, for this study the simulated radiances were assumed to be overcast through a plane-parallel RTM, and pixel sizes of AIRS and MODIS are assumed to be the same. Analysis of stand-alone AIRS retrievals favors SWIR channels, which were shown to be sensitive to COT and T_c through SVD analysis. AIRS SWIR and longwave CO_2 slicing channels are selected with comparable weight. Because of this, it is suggested that one should favor the longwave CO_2 slicing channels, in order to avoid non-LTE effects around 4.3 μm. However, it has been shown that the inclusion of SWIR CO_2 slicing channels aid AIRS temperature retrievals, which suggests that it might be worthwhile to include these channels for cloud temperature retrievals, provided that the proper correction for non-LTE effects are applied.

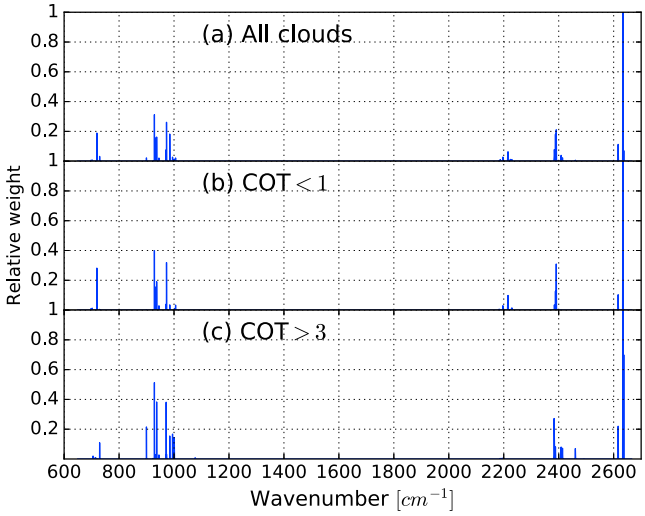

Figure 19. Relative weight of AIRS channels for (a) all clouds, (b) clouds with optical thickness less than 1, and (c) clouds with optical thickness larger than 3.

In the AIRS-only, MODIS-only, as well as AIRS+MODIS channel selections, the channel with highest IC rarely corresponds to cloud temperature information, echoing the finding of *Cooper et al.* [2003] which suggests that large errors in cloud boundaries will lead to significant uncertainties in other retrieved variables. Adding accurate cloud top boundary information from active sensors allows additional channels to be selected to improve COT and D_e retrievals. The results suggest that channel choices in presence of accurate cloud boundaries may not be as simple as taking away temperature retrieval channels but rather may allow new channels to contribute to COT and D_e retrievals owing to reduce uncertainty in cloud placement.

Having considered various permutations of satellite retrieval scenarios through varying surface type, viewing geometry, and cloud type, it is worthwhile to compile an optimal channel set from these IC analyses. Since the purpose of this study is to find the optimal channels for the most frequent cloud scenes, it is desirable to pick channels that contain the greatest information for clouds with larger populations, i.e., that are more common. Clustering analysis gives the occurrence frequency of each cloud type, which is used as weighting for the channel selection. Each cloud cluster center (used to represent a cloud type) has an associated population N_k representing the number of cloud profiles belonging to cluster k. We weight each channel by the number of clouds in each cluster,

$$W_\nu = \sum_k^K N_k f_\nu(k), \tag{20}$$

where

$$f_\nu(k) = \begin{cases} 1 & \text{if channel } \nu \text{ is selected for cluster } k, \\ 0 & \text{if channel } \nu \text{ is not selected for cluster } k, \end{cases} \tag{21}$$

W_ν is the weighting of the channel at wavelength ν, and K is the number of cloud types obtained from the clustering analysis. Such a weighting scheme gives preference to channels useful for clouds that occur more frequently. By using this weighting in conjunction with the channels selected objectively through IC analysis, we propose a recommended set of channels based on the IC channel selection.

The list of channels most heavily weighted for ice clouds retrievals is shown in Table 2, for three different retrieval scenarios, and Figure 19, categorized by COT. We find that for clouds with COT greater than 3, the CO_2 slicing channels around 700 and 2200 cm^{-1} (14.3 and 4.55 μm) have less weight than that of thinner clouds, indicating that these channels are useful mostly for thinner clouds. Conversely, within the window regions between 900 to 1000 cm^{-1} (11.1 to 10 μm) have larger weights for COT > 3. Aside from these differences, the spectral distribution of weighting is largely the same between the two COT categories. Based on this weighting, Table 2 provides a succinct channel set that is applicable to ice cloud retrievals over a wide range of scenes. Relative to the 59 channels used in the AIRS version 6 ice cloud retrieval [*Kahn et al.*, 2014], the channel set presented in Table 2 could potentially reduce computational expense, provided that retrieval experiments show that these channels can retrieve ice cloud properties with comparable accuracy to the retrievals done using the version 6 channel set.

In summary, this study has incorporated a large collection of observed ice cloud morphologies, together with varying satellite geometry and surface types, to obtain optimal channel sets for tropical ice cloud retrievals under three scenarios: a stand-alone AIRS algorithm, a combined AIRS-MODIS algorithm, and a combined active/passive retrieval that further utilizes cloud boundary information from CloudSat and CALIPSO. Although this paper has demonstrated the utility of IC for channel selection and analysis, one of the drawbacks of IC channel selection is the difficulty of properly representing uncertainties. While some uncertainties, such as ones due to temperature and humidity, are relatively straightforward to model, other error sources, such as non-LTE [*Strow et al.*, 2006], spatial inhomogeneity [*Kahn et al.*, 2015], and 3-D effects [*Fauchez et al.*, 2005] present significant challenges. Despite this drawback, IC channel selection provides a more robust assessment of optimal retrieval channels than simpler sensitivity analyses because it considers multiple sources of forward model uncertainties and prior knowledge of retrieved variables. The channel sets we have presented can serve as a guideline for optimal estimation ice cloud retrievals and will soon be tested in the AIRS version 6 algorithm.

Acknowledgments
The Cloud Properties and Radiative Heating Rates for TWP data set was obtained from http://www.arm.gov/data/pi/82 and the MERGESONDE products from http://www.arm.gov/data/vaps/mergesonde. AIRS SRFs are made available by the Atmospheric Spectroscopy Lab at the University of Maryland—Baltimore County (http://asl.umbc.edu/pub/airs/srf/srfhdf.html), and MODIS SRFs are provided by the Goddard Space Flight Center of NASA (http://mcst.gsfc.nasa.gov/calibration/parameters). A portion of this research was carried out at the Jet Propulsion Laboratory (JPL), California Institute of Technology, under a contract with the National Aeronautics and Space Administration. The AIRS version 6 and MODIS collection 6 data sets were processed by and obtained from the Goddard Earth Services Data and Information Services Center (http://daac.gsfc.nasa.gov/) and the Level 1 and Atmosphere and Archive Distribution System (http://ladsweb.nascom.nasa.gov). The authors were supported by the NASA Science of Terra and Aqua program under grant NNN13D455T.

References

Ackerman, T. P., and G. M. Stokes (2003), The atmospheric radiation measurement program, *Phys. Today*, *56*(1), 38–44, doi:10.1063/1.1554135.

Anderson, G., S. Clough, and F. Kneizys (1986), AFGL atmospheric constituent profiles, *Environ. Res. Pap.*, *954*, 1–46.

Aumann, H. H., et al. (2003), AIRS/AMSU/HSB on the aqua mission: Design, science objectives, data products, and processing systems, *IEEE Trans. Geosci. Remote Sens.*, *41*(2), 253–263, doi:10.1109/TGRS.2002.808356.

Baldridge, A. M., S. J. Hook, C. I. Grove, and G. Rivera (2009), The ASTER spectral library version 2.0, *Remote Sens. Environ.*, *113*(4), 711–715, doi:10.1016/j.rse.2008.11.007.

Barnes, W., T. Pagano, and V. Salomonson (1998), Prelaunch characteristics of the Moderate Resolution Imaging Spectroradiometer (MODIS) on EOS-AM1, *IEEE Trans. Geosci. Remote Sens.*, *36*(4), 1088–1100, doi:10.1109/36.700993.

Baum, B. A., P. Yang, A. J. Heymsfield, A. Bansemer, B. H. Cole, A. Merrelli, C. Schmitt, and C. Wang (2014), Ice cloud single-scattering property models with the full phase matrix at wavelengths from 0.2 to 100 μm, *J. Quant. Spectrosc. Radiat. Transfer*, *146*, 123–139, doi:10.1016/j.jqsrt.2014.02.029.

Bodhaine, B. A., N. B. Wood, E. G. Dutton, and J. R. Slusser (1999), On Rayleigh optical depth calculations, *J. Atmos. Oceanic Technol.*, *16*(11), 1854–1861, doi:10.1175/1520-0426(1999)016<1854:ORODC>2.0.CO;2.

Brewer, A. W. (1949), Evidence for a world circulation provided by the measurements of helium and water vapour distribution in the stratosphere, *Q. J. R. Meteorol. Soc.*, *75*(326), 351–363, doi:10.1002/qj.49707532603.

Chung, S., S. Ackerman, P. F. van Delst, and W. P. Menzel (2000), Model calculations and interferometer measurements of ice-cloud characteristics, *J. Appl. Meteorol.*, *39*(5), 634–644, doi:10.1175/1520-0450-39.5.634.

Comstock, J. M., A. Protat, S. A. McFarlane, J. Delanoë, and M. Deng (2013), Assessment of uncertainty in cloud radiative effects and heating rates through retrieval algorithm differences: Analysis using 3 years of ARM data at Darwin, Australia, *J. Geophys. Res. Atmos.*, *118*, 4549–4571, doi:10.1002/jgrd.50404.

Cooper, S. J., T. S. L'Ecuyer, and G. L. Stephens (2003), The impact of explicit cloud boundary information on ice cloud microphysical property retrievals from infrared radiances, *J. Geophys. Res.*, *108*(D3), 4107, doi:10.1029/2002JD002611.

Cooper, S. J., T. S. L'Ecuyer, P. Gabriel, A. J. Baran, and G. L. Stephens (2006), Objective assessment of the information content of visible and infrared radiance measurements for cloud microphysical property retrievals over the global oceans. Part II: Ice clouds, *J. Appl. Meteorol. Climatol.*, *45*(1), 42–62, doi:10.1175/JAM2327.1.

Cooper, S. J., T. S. L'Ecuyer, P. Gabriel, A. J. Baran, and G. L. Stephens (2007), Performance assessment of a five-channel estimation-based ice cloud retrieval scheme for use over the global oceans, *J. Geophys. Res.*, *112*, D04207, doi:10.1029/2006JD007122.

Divakarla, M. G., C. D. Barnet, M. D. Goldberg, L. M. McMillin, E. Maddy, W. Wolf, L. Zhou, and X. Liu (2006), Validation of atmospheric infrared sounder temperature and water vapor retrievals with matched radiosonde measurements and forecasts, *J. Geophys. Res.*, *111*, D09S15, doi:10.1029/2005JD006116.

Eldridge, R. G. (1967), Water vapor absorption of visible and near infrared radiation, *Appl. Opt.*, *6*(4), 709–713, doi:10.1364/AO.6.000709.

Fauchez, T., P. Dubuisson, C. Cornet, F. Szczap, A. Garnier, J. Pelon, and K. Meyer (2005), Impacts of cloud heterogeneities on cirrus optical properties retrieved from space-based thermal infrared radiometry, *Atmos. Meas. Tech.*, *8*, 633–647, doi:10.5194/amt-8-633-2015.

Fu, Q. (1996), An accurate parameterization of the solar radiative properties of cirrus clouds for climate models, *J. Clim.*, *9*(9), 2058–2082, doi:10.1175/1520-0442(1996)009<2058:AAPOTS>2.0.CO;2.

Gao, B.-C., A. F. H. Goetz, and W. J. Wiscombe (1993), Cirrus cloud detection from Airborne Imaging Spectrometer data using the 1.38 μm water vapor band, *Geophys. Res. Lett.*, *20*(4), 301–304, doi:10.1029/93GL00106.

Hale, G. M., and M. R. Querry (1973), Optical constants of water in the 200-nm to 200-microm wavelength region, *Appl. Opt.*, *12*(3), 555–563, doi:10.1364/AO.12.000555.

Hansen, J. E., and L. D. Travis (1974), Light scattering in planetary atmospheres, *Space Sci. Rev.*, *16*(4), 527–610, doi:10.1007/BF00168069.

Heymsfield, A. J., D. Winker, and G. J. van Zadelhoff (2005), Extinction-ice water content-effective radius algorithms for CALIPSO, *Geophys. Res. Lett.*, *32*, L10807, doi:10.1029/2005GL022742.

Hogan, R. J., M. E. Brooks, A. J. Illingworth, D. P. Donovan, C. Tinel, D. Bouniol, and J. P. V. P. Baptista (2006), Independent evaluation of the ability of spaceborne radar and lidar to retrieve the microphysical and radiative properties of ice clouds, *J. Atmos. Oceanic Technol.*, *23*(2), 211–227, doi:10.1175/JTECH1837.1.

Huang, H., P. Yang, H. Wei, B. A. Baum, Y. Hu, P. Antonelli, and S. Ackerman (2004), Inference of ice cloud properties from high spectral resolution infrared observations, *IEEE Trans. Geosci. Remote Sens.*, *42*(4), 842–853, doi:10.1109/TGRS.2003.822752.

Hsu, N.-C., R. Gautam, A. M. Sayer, C. Bettenhausen, C. Li, M. J. Jeong, S.-C. Tsay, and B. N. Holben (2012), Global and regional trends of aerosol optical depth over land and ocean using SeaWiFS measurements from 1997–2010, *Atmos. Chem. Phys.*, *12*(17), 8037–8053, doi:10.5194/acp-12-8037-2012.

Inness, A., et al. (2013), The MACC reanalysis: An 8 yr data set of atmospheric composition, *Atmos. Chem. Phys.*, *13*(8), 4073–4109, doi:10.5194/acp-13-4073-2013.

Inoue, T. (1985), On the temperature and effective emissivity determination of semi-transparent cirrus clouds by bi-spectral measurements in the 10 μm window region, *J. Meteorol. Soc. Jpn.*, *63*, 88–99.

Jensen, E. J., O. B. Toon, L. Pfister, and H. B. Selkirk (1996), Dehydration of the upper troposphere and lower stratosphere by subvisible cirrus clouds near the tropical tropopause, *Geophys. Res. Lett.*, *23*(8), 825–828, doi:10.1029/96GL00722.

Jin, H., and S. L. Nasiri (2014), Evaluation of AIRS cloud-thermodynamic-phase determination with CALIPSO, *J. Appl. Meteorol. Climatol.*, *53*(4), 1012–1027, doi:10.1175/JAMC-D-13-0137.1.

Kahn, B. H., A. Eldering, M. Ghil, S. Bordoni, and S. A. Clough (2004), Sensitivity analysis of cirrus cloud properties from high-resolution infrared spectra. Part I: Methodology and synthetic cirrus, *J. Clim.*, *17*(24), 4856–4870, doi:10.1175/JCLI-3220.1.

Kahn, B. H., et al. (2014), The Atmospheric Infrared Sounder version 6 cloud products, *Atmos. Chem. Phys.*, *14*(1), 399–426, doi:10.5194/acp-14-399-2014.

Kahn, B. H., M. M. Schreier, Q. Yue, E. J. Fetzer, F. W. Irion, S. Platnick, C. Wang, S. L. Nasiri, and T. S. L'Ecuyer (2015), Pixel-scale assessment and uncertainty analysis of AIRS and MODIS ice cloud optical thickness and effective radius, *J. Geophys. Res. Atmos.*, *120*, 11,669–11,689, doi:10.1002/2015JD023950.

L'Ecuyer, T. S., P. Gabriel, K. Leesman, S. J. Cooper, and G. L. Stephens (2006), Objective assessment of the information content of visible and infrared radiance measurements for cloud microphysical property retrievals over the global oceans. Part I: Liquid clouds, *J. Appl. Meteorol. Climatol.*, *45*(1), 20–41, doi:10.1175/JAM2326.1.

Lensky, I. M., and D. Rosenfeld (2008), Clouds-Aerosols-Precipitation Satellite Analysis Tool (CAPSAT), *Atmos. Chem. Phys.*, *8*(22), 6739–6753, doi:10.5194/acp-8-6739-2008.

Liou, K. (1986), Influence of cirrus clouds on weather and climate processes: A global perspective, *Mon. Weather Rev.*, *114*, 1167–1198.
Moran, K. P., B. E. Martner, M. J. Post, R. A. Kropfli, D. C. Welsh, and K. B. Widener (1998), An unattended cloud-profiling radar for use in climate research, *Bull. Am. Meteorol. Soc.*, *79*(3), 443–455, doi:10.1175/1520-0477(1998)079<0443:AUCPRF>2.0.CO;2.
Nakajima, T., and M. D. King (1990), Determination of the optical thickness and effective particle radius of clouds from reflected solar radiation measurements. Part I: Theory, *J. Atmos. Sci.*, *47*(15), 1878–1893, doi:10.1175/1520-0469(1990)047<1878:DOTOTA>2.0.CO;2.
Rodgers, C. D. (1976), Retrieval of atmospheric temperature and composition from remote measurements of thermal radiation, *Rev. Geophys. Space Phys.*, *14*(4), 609–624, doi:10.1029/RG014i004p00609.
Rodgers, C. D. (1996), Information content and optimization of high-spectral-resolution measurements, *Proc. SPIE Opt. Spectrosc. Tech. Instrum. Atmos. Space Res. II*, *2830*(97), 136–147.
Rodgers, C. D. (2000), *Inverse Methods for Atmospheric Sounding: Theory and Practice, Ser. on Atmos., Oceanic and Planet. Phys.*, World Sci., Singapore.
Rothman, L. S., et al. (2009), The HITRAN 2008 molecular spectroscopic database, *J. Quant. Spectrosc. Radiat. Transfer*, *110*(9–10), 533–572, doi:10.1016/j.jqsrt.2009.02.013.
Sassen, K., Z. Wang, and D. Liu (2008), Global distribution of cirrus clouds from CloudSat/Cloud-Aerosol Lidar and Infrared Pathfinder Satellite Observations (CALIPSO) measurements, *J. Geophys. Res.*, *113*, D00A12, doi:10.1029/2008JD009972.
Sassen, K., Z. Wang, and D. Liu (2009), Cirrus clouds and deep convection in the tropics: Insights from CALIPSO and CloudSat, *J. Geophys. Res.*, *114*, D00H06, doi:10.1029/2009JD011916.
Shannon, C. E., and W. Weaver (1949), The mathematical theory of communication, *Math. Theory Commun.*, *27*(4), 117, doi:10.2307/3611062.
Sidran, M. (1981), Broadband reflectance and emissivity of specular and rough water surfaces, *Appl. Opt.*, *20*(18), 3176–3183, doi:10.1364/AO.20.003176.
Smith, W. L., and C. M. R. Platt (1978), Comparison of satellite-deduced cloud heights with indications from radiosonde and ground-based laser measurements, *J. Appl. Meteorol.*, *17*, 1796–1802, doi:10.1175/1520-0450(1978)017<1796:COSDCH>2.0.CO;2.
Sofieva, V. F. (2003), Information approach to optimal selection of spectral channels, *J. Geophys. Res.*, *108*(D16), 4513, doi:10.1029/2002JD002980.
Sourdeval, O., L.-C. Labonnote, A. J. Baran, and G. Brogniez (2015), A methodology for simultaneous retrieval of ice and liquid water cloud properties. Part I: Information content and case study, *Q. J. R. Meteorol. Soc.*, *141*(688), 870–882, doi:10.1002/qj.2405.
Spinhirne, J. D. (1993), Micro pulse lidar, *IEEE Trans. Geosci. Remote Sens.*, *31*(1), 48–55, doi:10.1109/36.210443.
Spurr, R. J. D. (2006), VLIDORT: A linearized pseudo-spherical vector discrete ordinate radiative transfer code for forward model and retrieval studies in multilayer multiple scattering media, *J. Quant. Spectrosc. Radiat. Transfer*, *102*(2), 316–342, doi:10.1016/j.jqsrt.2006.05.005.
Stephens, G. L., et al. (2008), CloudSat mission: Performance and early science after the first year of operation, *J. Geophys. Res.*, *13*, D00A18, doi:10.1029/2008JD009982.
Strow, L. L., S. E. Hannon, S. De-Souza Machado, H. E. Motteler, and D. C. Tobin (2006), Validation of the atmospheric infrared sounder radiative transfer algorithm, *J. Geophys. Res.*, *111*, D09S06, doi:10.1029/2005JD006146.
Susskind, J., J. M. Blaisdell, and L. Iredell (2014), Improved methodology for surface and atmospheric soundings, error estimates, and quality control procedures: The atmospheric infrared sounder science team version-6 retrieval algorithm, *J. Appl. Remote Sens.*, *8*(1), 08499, doi:10.1117/1.JRS.8.084994.
Troyan, D. (2012), Merged sounding value-added product, *Tech. Rep. DOE/SC-ARM/TR-087*, US Department of Energy, Washington, D. C. [Available at https://www.arm.gov/publications/tech_reports/doe-sc-arm-tr-087.pdf.]
Wang, C., S. Platnick, Z. Zhang, K. Meyer, G. Wind, and P. Yang (2016a), Retrieval of ice cloud properties using an optimal estimation algorithm and MODIS infrared observations: 2. Retrieval evaluation, *J. Geophys. Res. Atmos.*, *121*, 5827–5845, doi:10.1002/2015JD024528.
Wang, C., S. Platnick, Z. Zhang, K. Meyer, and P. Yang (2016b), Retrieval of ice cloud properties using an optimal estimation algorithm and MODIS infrared observations: 1. Forward model, error analysis, and information content, *J. Geophys. Res. Atmos.*, *121*, 5809–5826, doi:10.1002/2015JD024526.
Wang, Z., and K. Sassen (2002), Cirrus cloud microphysical property retrieval using lidar and radar measurements. Part II: Midlatitude cirrus microphysical and radiative properties, *J. Atmos. Sci.*, *59*(14), 2291–2302, doi:10.1175/1520-0469(2002)059<2291:CCMPRU>2.0.CO;2.
Wilks, D. (1997), *Series Editors, International Geophysics Series*, Academic Press, New York, doi:10.1016/S0074-7742(08)60337-2.
Xiong, X., J.-Q. Sun, J. A. Esposito, B. Guenther, and W. L. Barnes (2003a), MODIS reflective solar bands calibration algorithm and on-orbit performance, *Proc. SPIE*, *4891*, 95–104, doi:10.1117/12.466096.
Xiong, X., K. Chiang, B. Guenther, and W. L. Barnes (2003b), MODIS thermal emissive bands calibration algorithm and on-orbit performance, *Proc. SPIE*, *4891*, 392–401, doi:10.1117/12.466083.
Yang, P., L. Bi, B. A. Baum, K.-N. Liou, G. W. Kattawar, M. I. Mishchenko, and B. Cole (2013), Spectrally consistent scattering, absorption, and polarization properties of atmospheric ice crystals at wavelengths from 0.2 to 100 μm, *J. Atmos. Sci.*, *70*(1), 330–347, doi:10.1175/JAS-D-12-039.1.